FACULDADE DE ENGENHARIA DA UNIVERSIDADE DO PORTO

Turbulent Flow Around a Square Cylinder: a Comparative Numerical Study

Tiago Manuel Azevedo Ferreira

Master Degree in Mechanical Engineering

Supervisor: Fernando Tavares De Pinho

Co-Supervisor: Alexandre Miguel Prior Afonso

April 01, 2020

Turbulent Flow Around a Square Cylinder: a Comparative Numerical Study

Tiago Manuel Azevedo Ferreira

Master Degree in Mechanical Engineering

April 01, 2020

Resumo

O escoamento viscoso em torno de um cilindro é um tema clássico de simulação computacional com uma grande importãncia em vários setores da aerodinâmica.

Simulações bidimensionais de um escoamento turbulento em torno de um cilindro quadrangular com $Re = 21400$ são o foco de estudo desta dissertação. As simulações efetuadas são usadas como base para uma análise comparativa entre a performance dos vários modelos de turbulência usados. O objetivo do estudo é a realização de uma discussão que relacione os pontos positivos e negativos das várias topologias de modelos adotados.

As propriedades usadas como base de comparação são o coeficiente de arrasto, o número de Strouhal correspondente à frequência de oscilação do escoamento, os perfis de velocidade e de energia cinética turbulenta a jusante do cilindro, as linhas de corrente e as isolinhas de energia cinética.

Foram usados três tipos de modelos de CFD: modelos lineares de viscosidade turbulenta, modelos de tensão de Reynolds e modelos de baixo número de Reynolds.

Apesar dos resultados numéricos obtidos pelos modelos de tensão de Reynolds estarem mais próximos dos dados publicados, a principal conclusão do estudo foi a de que os modelos $k-\omega$ SST e $k-\omega$ SSTLM (ambos modelos lineares de viscosidade turbulenta) apresentaram o melhor conjunto de resultados nas diferentes propriedades avaliadas.

O *OpenFOAM* foi o software usado para as simulações efetuadas.

Abstract

The viscous flow around cylinders is a classic CFD simulation setup with major importance in various sectors of aerodynamics.

This dissertation focuses on the numerical assessment of several turbulence models in a turbulent flow around a square cylinder with $Re = 21400$. The results from the simulations are used as comparative terms for the performance evaluation of the various turbulence models used. The goal of this study is to discuss the advantages and disadvantages offered by the various typologies of existing CFD models.

The flow properties evaluated are the drag coefficient, the Strouhal number correspondent to the flow shedding frequency , the velocity and turbulent kinetic energy profiles downstream of the cylinder and the velocity streamlines and kinetic energy contours.

We used three types of CFD models: linear eddy viscosity turbulence models, Reynolds stresses turbulence models and low Reynolds number turbulence models.

Although the numerical results attained from the Reynolds stress models were the closest to the published data, the overall results given by $k-\omega$ SST and $k-\omega$ SSTLM (both linear eddy viscosity models) gave the best flow description in the aggregate of the properties measured.

OpenFOAM was the software used for the CFD simulations.

Acknowledgments

There are many people to whom I owe eternal gratitude for the guidance, support and companionship. Without these people this project certainly would not be possible.

To my supervisor, professor Fernando Tavares de Pinho, for the availability and constant advice, both fundamental for the realization of this work.

To my co-supervisor, professor Alexandre Miguel Prior Afonso, for the constant preoccupation on the work progress and for the help given in every step of the way in solving even the simplest of problems.

To my family to whom I owe everything I have and the person I became. Your light resonates with me everyday.

To every person I crossed path with the last five years on the various weekend jobs: you taught me more than knowledge, you showed me how to be resilient and kind. A special thanks to the Xis Snack bar staff, particularly to Nuno, Linda, Sérgio, Neusa, Adriana and Filipa: your happiness and responsibility inspire me every day.

To my hometown friends Catarina Mendes and Micael Torres that still have the patience to put up with me.

To my Erasmus friends that I always carry in my heart.

To my neighbours and friends Diogo Boavida, Eduardo Miranda, Francisco Teixeira, João Pinto, Marco Pinto Coelho, Pedro Sá and Tiago Abreu for the companionship and friendship over the last years.

I wish you more than luck.

Thank you all.

Tiago Ferreira

I like it when somebody gets excited about something. It’s nice.

J.D. Salinger

Contents

List of Figures

List of Tables

Nomenclature

δ_{ij}	Kronecker delta
γ	Intermittency factor
μ	Dynamic viscosity
ν	Kinematic viscosity $\left(\frac{\mu}{\rho}\right)$
ν_T	Turbulent viscosity
$\overline{S}_{ij}$	Mean rate of strain tensor $\frac{1}{2}\left(\frac{\partial \overline{u}_i}{\partial x_j} + \frac{\partial \overline{u}_j}{\partial x_i}\right)$
$\overline{u_i' u_j'}$	Reynolds averaged Reynolds stresses
$\overline{u}(x,t)$	Reynolds averaged velocity field
ρ	Density $[kg/m^3]$
τ_w	Wall shear stress
τ_{ij}	Reynolds stress tensor
C_d	Drag Coefficient
C_L	Lift Coefficient
f	Shedding frequency [Hz]
k	Turbulent kinetic energy $(\frac{1}{2}\overline{u_i' u_i'})$
L	Characteristic cylinder dimension
Re	Reynolds number $\left(\frac{U_o L}{\nu}\right)$
Re_θ	Strain rate Reynolds number $\left(\frac{y^2 S}{\nu}\right)$
S_{ij}	Rate of strain tensor $\frac{1}{2}\left(\frac{\partial u_i}{\partial x_j} + \frac{\partial u_j}{\partial x_i}\right)$
s_{ij}	Fluctuating rate of strain
St	Strouhal number $\left(\frac{f U_o}{L}\right)$
u'	Fluctuating velocity field

$u(x,t)$	Instantaneous velocity field
u^+	Non-dimensional velocity $\left(\frac{u}{u_\tau}\right)$
u_τ	Friction velocity $\left(\sqrt{\frac{\tau_w}{\rho}}\right)$
U_o	Inlet flow velocity
y^+	Non-dimensional wall distance $\left(\frac{yu_\tau}{\nu}\right)$
ε	Rate of dissipation of turbulent kinetic energy $(2\nu \cdot \overline{s_{ij}s_{ij}})$
ω	Specific rate of dissipation of turbulent kinetic energy $\left(\frac{\varepsilon}{k}\right)$
$\overline{p}$	Reynolds averaged pressure field

Abbreviations

CFD	Computational fluid dynamics
LES	Large-eddy simulation
DNS	Direct Numerical Simulations
RANS	Reynolds-averaged Navier -tokes
LRR	Reynolds-stress model of Launder, Reece, and Rodi
SSG	Reynolds-stress model of Speziale, Sarkar and Gatski

Chapter 1

Introduction

Turbulence is a physical phenomenon that occurs naturally in flows above a critical condition characterized by the chaotic change of field values in time and space. Because of its prevalence in many engineering applications, the correct prediction of turbulence is essential in engineering tools.

The purpose of this thesis is to make a comparative numerical assessment of several existing turbulence models through the simulation of a turbulent flow past a square cylinder.

High Reynolds number turbulence is characterized by a wide range of spatial and temporal scales. The most accurate way to simulate turbulent flow is to solve the Navier-Stokes (NS) equations for the instantaneous quantities, the so-called direct numerical simulation (DNS). Despite the numerical accuracy, this procedure is impractical for high Reynolds number flows of practical interest, specially when performing parametric assessments carrying a large computational cost that might not be economically viable. Therefore, in industrial applications engineers resorts to modelling approaches. The most common modelling tool in industry relies on the Reynolds-averaged Navier-Stokes (RANS) formulation which are also called Reynolds equations. Using this technique the different quantity fields are decomposed into the mean component and the fluctuations around this mean. The equations are then solved for the mean field and the effect of the fluctuations on the mean quantities is modelled. In this way it is not necessary to solve most turbulent scales and the computational cost is significantly reduced.

1.1 Existing literature

The flow around a square cylinder constitutes a classical configuration to study the flow around bluff bodies. The main features of this flow are presented in schematically in figure 1.1. At high Reynolds number the flow separates preferably from the upstream sharp cylinder corners and a separation bubble is formed along the edge and at the rear of the cylinder. The asymmetric shedding of the produced vortices into the wake induces forces on the cylinder leading to structural vibration. Such vibration is termed Vortex-Induced Vibration. This fluid excitation forms a potent source of fatigue and flow-induced noise for many engineering applications. Towering structures,

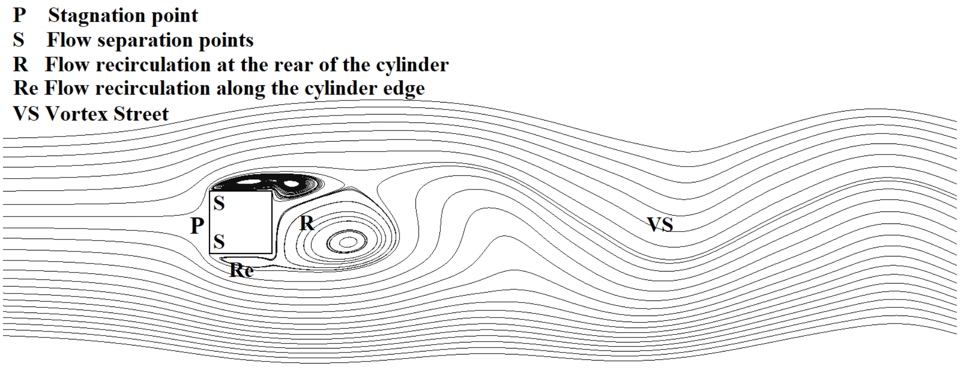

Figure 1.1: Sketch of main features present in the turbulent flow around a square cylinder

skyscrapers, marine riser pipes, long-spanned bridges and wires are examples thereof. The pulsating flow pattern at the rear of the cylinder forms what is called a Vortex street, composed by symmetrically disposed vortices along the streamline center.

The majority of research on flow around cylindrical objects has been carried out for circular cylinders. The main difference between this setup and the square cylinder is that in the former configuration separation points are time-dependent.

The turbulent wake around a square cylinder was studied experimentally using laser-Doppler measurements by Lyn et al. (1995). This results were crucial for the validity assessment of our results. Furthermore several DNS and LES studies have been published for this configuration providing a good agreement with experimental results. The DNS results attained by Trias et al. (2015) and the LES measurements attained by Sohanker et al. (2000) and Minguez et al. (2011) are used for comparison purposes with the numerical results attained from our simulations. Also, the results by Lyn in 1990, attained from Franke and Rodi (1991), are used for comparison of the turbulent kinetic energy calculated downstream of the flow.

This thesis will be organised as follows:

- Chapter 2 gives an overview on the major turbulence models used in industry, their modelling equations, wall functions and model features and their implications in the validity of the solutions attained;
- Chapter 3 briefly presents the numerical methods and all the numerical schemes and solvers used in the simulations;
- Chapter 4 presents and discusses the results obtained for the laminar and turbulent flow simulations;
- Finally, the thesis closes in chapter 5 with a summary of the main conclusions and an appraisal of what could be done in the future to complete this comparative study.

Chapter 2

Mathematical models

This chapter begins with an overview on the equations governing turbulent flows around bluff bodies. Subsequently, the turbulence models used in the simulations for this project are presented.

2.1 Governing equations

The velocity field of a turbulent flow $u(x,t)$ may be decomposed into its mean $\overline{u}(x,t)$ and the fluctuations $u'(x,t)$:

$$u(x,t) = \overline{u}(x,t) + u'(x,t) \tag{2.1}$$

The fundamental equations that govern the incompressible, isothermal and turbulent flow of a Newtonian fluid are the Navier-Stokes equations. Introducing the Reynolds decomposition (2.1) into those equations we arrive at equations (2.2) - the Reynolds equations. This equations have an extra term on the right hand side - the Reynolds stresses - that appears due to momentum transfer by the fluctuating velocity field $u'(x,t)$. The mean velocity field $\overline{u}(x,t)$ is governed by the Reynolds equation (2.2) and the continuity equation (2.3):

$$\frac{\partial \overline{u}_i}{\partial t} + \overline{u}_j \frac{\partial \overline{u}_i}{\partial x_j} = \nu \frac{\partial}{\partial x_j}\left(\frac{\partial \overline{u}_i}{\partial x_j} + \frac{\partial \overline{u}_j}{\partial x_i}\right) - \frac{\partial \overline{u'_i u'_j}}{\partial x_i} - \frac{1}{\rho}\frac{\partial \overline{p}}{\partial x_i} \tag{2.2}$$

$$\frac{\partial \overline{u}_i}{\partial x_i} = 0 \tag{2.3}$$

where $\overline{p}$ is the average pressure field, ρ is the flow density, ν is the fluid viscosity and t represents time.

The right hand side of equation (2.2) represents the sum of three stresses acting on the control volume: the viscous extra stress, the Reynolds stresses and the isotropic stress quantified by the pressure. The Reynolds stresses arise from momentum transfer by the fluctuating velocity field. This term represents the only difference between equation (2.2) and the Navier-Stokes equations (in addition to the fact that equation (2.2) deals with Reynolds-averaged quantities whereas the NS equations deal with instantaneous quantities).

For a statistically three-dimensional flow, there are four independent governing equations: the three components of the Reynolds equations (eq. 2.2) together with the continuity equation (eq. 2.3). However, these four equations contain more than four unknowns. In addition to the three components of the velocity vector $\overline{u}$ and $\overline{p}$ there are also the six components of the symmetric Reynolds stress tensor, according to Pope (2000). The system of equations cannot be solved without somehow determining those six Reynolds stresses, the system is said to be unclosed. The different turbulence models were developed to give a closure to this problem, providing the additional six equations in order for the number of unknowns to be equal to the number of equations.

In a turbulent flow simulation, equations are solved for a time-dependent velocity field that, to some extent, represents the velocity field $u(x,t)$ for one realisation of the turbulent flow (Pope, 2000). The most used simulation techniques are DNS and large eddy simulation (LES).

On the other hand, in a turbulence model, a set of equations are provided for all components of the Reynolds stress tensor. In some models, that set of equations depend on some mean flow quantities whereas in others, the Reynolds stresses are modelled as transport equations. This approach is called RANS (Reynolds averager Navier-Stokes).

The application of RANS turbulence models discards all details concerning the state of the flow contained in the instantaneous fluctuations, according to Versteeg and Malalasekera (2007). The most commonly used RANS models are the linear eddy viscosity models and the Reynolds stress models. Whilst the first obtains the Reynolds stresses through an algebraic relation that depends on such quantities as the turbulence dissipation (ε) and the turbulent kinetic energy (k), in the second approach the Reynolds stresses are modelled directly through six transport equations (Pope, 2000).

One problem that crosses all turbulence models is their poor description of near wall flow behaviour. In fact, turbulence models are developed for high Reynolds number flow turbulence. Close to walls, however, the local Reynolds number goes down as it is proportional to the wall distance and the model cannot predict a correct flow behaviour. This issue is surpassed by the use of wall functions in those regions of the flow.

The choice in wall treatment usually encompasses either wall functions (RANS models) or integration until the surface wall, using a low Reynolds number Re formulation, according to Menter and Esch (2001). In most industrial CFD simulations, a wall function approach is used. This function bridges the viscous sub-layer to conditions imposed at the wall. This approach makes use of coarse near-wall grids in such a way that the first layer of cells is located in the logarithmic region. This way, it is assumed that the first grid point is located in the fully developed flow region, in the sense of a turbulent boundary layer, even though in reality it is not. In contrast, in a low Re formulation the mesh goes down to the wall and needs to be fine enough to resolve the mean flow field in the vicinity to the wall, leading to a more expensive calculation.

Some CFD software provide an hybrid solution. They have automatic near-wall treatment for specific dissipation equation based models. This method switches automatically from a wall function to a low-Re formulation based on the grid density provided by the user. It ensures therefore an optimal accuracy of the CFD solution on a given grid (Menter and Esch, 2001).

For a turbulence model to be useful in a general-purpose CFD code it must have wide applicability, be accurate, simple and economical to run (Versteeg and Malalasekera, 2007).

The aim of this thesis is not to develop turbulence models but instead to use several in a single complex flow, the flow around a square cylinder. The model descriptions given below are thereby aimed at informing the reader about the full set of equations used, as well as a brief description on their advantages and disadvantages. This is not aimed to a be a fully exhaustive description of turbulence models.

2.2 Linear eddy viscosity turbulence models

Eddy viscosity models are based on the Boussinesq assumption (equation 2.4) that an alignment exists between the deviatoric Reynolds stresses and the mean strain tensor ($\overline{S}_{ij}$) (Pope, 2000). They presume that the shear stress vector is aligned with the velocity gradient vector and that the normal Reynolds stresses are equal, according to Lee et al. (2000).

$$-\rho\overline{u'_i u'_j} + \frac{2}{3}\rho k\delta_{ij} = \rho\nu_T\left(\frac{\partial\overline{u}_i}{\partial x_j} + \frac{\partial\overline{u}_j}{\partial x_i}\right) = 2\rho\nu_T\overline{S}_{ij} \tag{2.4}$$

$$\rho\overline{u'_i u'_j} = \begin{bmatrix} \overline{u'^2_x} & \overline{u'_x u'_y} & \overline{u'_x u'_z} \\ \overline{u'_y u'_x} & \overline{u'^2_y} & \overline{u'_y u'_z} \\ \overline{u'_z u'_x} & \overline{u'_z u'_y} & \overline{u'^2_z} \end{bmatrix} \tag{2.5}$$

The turbulence kinetic energy k (eq. 2.6) is the mean kinetic energy per unit mass in the fluctuating velocity field (u'_i). It is also half the trace of the Reynolds stress tensor (relation 2.5).

$$k = \frac{1}{2}\overline{u'_i u'_i} \tag{2.6}$$

Turbulence dissipation ε (2.7) is defined as the rate of dissipation of turbulent kinetic energy. This property emerges from the work the fluctuating velocity gradients do against the fluctuating deviatoric stresses ($2\nu s_{ij}$), transforming kinetic energy into internal energy (Pope, 2000).

$$\varepsilon = 2\nu\overline{s_{ij}s_{ij}} \tag{2.7}$$

The eddy viscosity (ν_T) is the turbulent analogous of the kinematic molecular viscosity (ν). The analogy stands on the assumption that, just as in the molecular processes, there is a proportionality between the shear stress and the mean velocity gradient.

Nevertheless, the physics of turbulence is vastly different than the physics of molecular processes that lead to the viscous stress law. That said, evidence suggests that the turbulent viscosity hypothesis is quite reasonable for simple shear flows.

The specific dissipation rate ω is defined by equation (2.8).

$$\omega = \frac{\varepsilon}{k} \tag{2.8}$$

The different eddy viscosity models solve transport equations for turbulence properties such as k and ε, which in turn are constituted by many terms that require modelling. Below it is presented the various turbulence models that exist in the openFoam catalogue and that was used in the numerical simulations.

2.2.1 The k-ε model

The $k-\varepsilon$ model was presented in 1973 by Launder and Spalding (1974), and is constituted by two transport equations: one for the turbulent kinetic energy (eq. 2.9) and another for the rate of dissipation of turbulent kinetic energy (eq. 2.10) that determine k and ε, respectively, which are then used to quantify the eddy viscosity.

For this turbulence model, the turbulent eddy viscosity (ν_T) is computed through the algebraic relation (2.11) and the coefficients of this model are presented in table 2.1.

$$\frac{\partial k}{\partial t} + \bar{u}_j \frac{\partial k}{\partial x_j} = \tau_{ij} \frac{\partial \bar{u}_i}{\partial x_j} - \varepsilon + \frac{\partial}{\partial x_j}\left[\left(\nu + \frac{\nu_T}{\sigma_k}\right)\frac{\partial k}{\partial x_j}\right] \tag{2.9}$$

$$\frac{\partial \varepsilon}{\partial t} + \bar{u}_j \frac{\partial \varepsilon}{\partial x_j} = C_{\varepsilon 1} \frac{\varepsilon}{k} \tau_{ij} \frac{\partial \bar{u}_i}{\partial x_j} - C_{\varepsilon 2} \frac{\varepsilon^2}{k} + \frac{\partial}{\partial x_j}\left[\left(\nu + \frac{\nu_T}{\sigma_\varepsilon}\right)\frac{\partial k}{\partial x_j}\right] \tag{2.10}$$

$$\nu_T = C_\mu \frac{k^2}{\varepsilon} \tag{2.11}$$

Table 2.1: Constants used on the k-ε model (equations (2.11), (2.9) and (2.10), according to Launder and Spalding (1974))

C_μ	$C_{\varepsilon 1}$	$C_{\varepsilon 2}$	σ_k	σ_ε
0.09	1.44	1.92	1.0	1.3

This model is usually preferred for high Reynolds number applications. It is a robust, widely used, easy to implement and computationally cheap turbulence model.

Despite its massive usage, this model performs poorly for complex flows involving adverse pressure gradients, flow separation and strong streamline curvature. Another common criticism lies on its poor flow description near walls and the consequent necessity for the implementation of wall functions. There are many wall functions published over the years which lead to an improved agreement with DNS data.

2.2.2 The $k-\omega$ model

The $k-\omega$ turbulence model was first postulated by Kolmogorov in 1942 and later independently by Saffman in 1970. This model also has an equation for k (equation 2.13), but relies on an equation for the so-called specific dissipation rate, ω (equation 2.14) instead of the equation for ε. Consequently, for this model, the eddy viscosity (ν_T) is attained through equation (2.12).

$$\nu_T = \frac{k}{\omega} \tag{2.12}$$

The transport equations presented below are those presented by Wilcox (2008).

$$\frac{\partial k}{\partial t} + \frac{\partial}{\partial x_j}(u_j k) = \tau_{ij}\frac{\partial \bar{u}_i}{\partial x_j} - \beta^* k\omega + \frac{\partial}{\partial x_j}\left[\left(\nu + \sigma^* \frac{k}{\omega}\right)\frac{\partial k}{\partial x_j}\right] \tag{2.13}$$

$$\frac{\partial \omega}{\partial t} + \bar{u}_j\frac{\partial \omega}{\partial x_j} = \alpha\frac{\omega}{k}\tau_{ij}\frac{\partial \bar{u}_i}{\partial x_j} - \beta\omega^2 + \frac{\partial}{\partial x_j}\left[\left(\nu + \sigma\frac{k}{\omega}\right)\frac{\partial \omega}{\partial x_j}\right] \tag{2.14}$$

$$\beta = \beta_o f_\beta, \qquad f_\beta = \frac{1+85\chi_\omega}{1+100\chi_\omega} \tag{2.15}$$

$$\chi_\omega = \left|\frac{\Omega_{ij}\Omega_{jk}\hat{S}_{ki}}{(\beta^*\omega)^3}\right|, \qquad \hat{S}_{ki} = S_{ki} - \frac{1}{2}\frac{\partial u_m}{\partial x_m}\delta_{ki} \tag{2.16}$$

Table 2.2: Constants used on the k-ω model (equations (2.12), (2.13) and (2.14), according to Pope (2000) and Wilcox (2008))

C_μ	β_o	β^*	α	σ	σ^*
0.09	0.0708	0.09	0.52	0.5	0.6

The $k-\omega$ model is the preferable near wall choice as it accurately predicts the turbulent length scale in adverse pressure gradient flows according to Menter and Esch (2001). Furthermore, the model has a very simple low-Re formulation, which does not require additional non-linear wall damping terms. In this way, the simple Dirichlet boundary condition can be directly specified, according to Menter (1994). The coefficients of the model are listed in table 2.2.

This model is appraised for its simplicity, numerical stability and robustness. It demonstrates a good performance for wall-bounded boundary layer, free shear, and low Reynolds number flows.

The main deficiency of the standard $k-\omega$ is its strong sensitivity to free-stream values of ω_f outside the boundary layer, according to Menter (1992). Furthermore, the model does not accurately represent the k distribution and it underestimates the amount of separation for severe adverse pressure gradient flows.

So, both $k-\varepsilon$ and $k-\omega$ models do not show an accurate performance for flow separation from a smooth surface when compared to experimental measurements. This is mainly due to overestimation of wall shear stress.

2.2.3 The hybrid $k-\omega$ Shear Stress Transport (SST) model

Some of the advantages and deficiencies of the $k-\varepsilon$ and $k-\omega$ models are somewhat complementary and this finding fostered the development of a hybrid turbulence model, the k-ω SST turbulence model which emerged to improve upon the advantages presented by the $k-\omega$ and $k-\varepsilon$ individually. This model combines the best features of both models through the use of a blending function F_1 (equation 2.21).

For this model, the computation of the eddy viscosity follows equation (2.17).

$$\nu_T = \frac{a_1 k}{max(a_1\omega;\Omega F_2)} \tag{2.17}$$

where Ω is the absolute value of vorticity and function F_2 is attained through equation (2.18).

$$F_2 = tanh\left(arg_2^2\right); \qquad arg_2 = max\left(2\frac{\sqrt{k}}{\beta^*\omega y};\frac{500\nu}{y^2\omega}\right) \tag{2.18}$$

The eddy viscosity needs k and ω given by their transport equations, equations (2.19) and (2.20), respectively.

$$\frac{\partial k}{\partial t} + \bar{u}_j\frac{\partial k}{\partial x_j} = min\left(\tau_{ij}\frac{\partial \bar{u}_i}{\partial x_j};c_1\varepsilon\right) - \beta^* k\omega + \frac{\partial}{\partial x_j}\left[\left(\nu + \frac{\nu_t}{\sigma_k}\right)\frac{\partial k}{\partial x_j}\right] \tag{2.19}$$

$$\frac{\partial \omega}{\partial t} + \bar{u}_j\frac{\partial \omega}{\partial x_j} = \frac{\gamma}{\nu_t}\tau_{ij}\frac{\partial \bar{u}_i}{\partial x_j} - \beta\omega^2 + 2(1-F_1)\sigma_{\omega_2}\frac{1}{\omega}\frac{\partial k}{\partial x_j}\frac{\partial \omega}{\partial x_j} + \frac{\partial}{\partial x_j}\left[\left(\nu + \frac{\nu_t}{\sigma_k}\right)\frac{\partial \omega}{\partial x_j}\right] \tag{2.20}$$

The ω equation is similar to equation (2.14), with the exception of an extra term on the right hand side (the cross diffusion term) containing the damping function F_1. This term arises during the $\varepsilon = k\omega$ transformation of the diffusion term in the ε equation.

$$F_1 = tanh\left(arg_1^4\right); \qquad arg_1 = min\left[max\left(\frac{\sqrt{k}}{\beta^*\omega y};\frac{500\nu}{y^2\omega}\right);\frac{4\rho\sigma_{\omega 2}k}{CD_{k\omega}y^2}\right] \tag{2.21}$$

$$CD_{k\omega} = max\left(2\rho\sigma_{\omega 2}\frac{1}{\omega}\frac{\partial k}{\partial x_j}\frac{\partial \omega}{\partial_j}, 10^{-10}\right) \tag{2.22}$$

The term arg_1 (equation 2.21) goes to zero away from the solid surfaces. Consequently $F_1 = 0$ in the outer region of the flow, while $F_1 = 1$ near the surface wall. As a result, the $k-\omega$ model is recovered close to walls and the $k-\varepsilon$ appears far from walls.

The combined coefficients ϕ used in this model are calculated from the coefficients ϕ_1 and ϕ_2 according to equation (2.23) and tables (2.3) and (2.4) for ϕ_1 and ϕ_2 respectively.

$$\phi = F_1\phi_1 + (1-F_1)\phi_2 \tag{2.23}$$

The k-ω SST model shows a significant improvement for the individual $k-\varepsilon$ and $k-\omega$ models for cases involving adverse pressure gradients and is one of the preferred models for aerodynamic

Table 2.3: Constants ϕ_1 for the $k-\omega$ SST model

σ_{k1}	σ_{ω_1}	β_1	β^*	a_1	k	γ_1	c_1
1.176	2	0.0750	0.09	0.31	0.41	0.5532	10

Table 2.4: Constants ϕ_2 for the $k-\omega$ SST model

σ_{k2}	σ_{ω_2}	β_2	β^*	a_1	k	γ_2
1.0	1.168	0.0828	0.09	0.31	0.41	0.4403

applications (Menter, 1994). Despite the increased programming effort this model requires in comparison with the simpler $k-\varepsilon$ and $k-\omega$ models, it consumes little more computing time than each of them, while being very stable, even in complex applications. That is justified by the fact that this model has the same number of differential equations to be solved, which is the expensive part of a turbulence model.

The introduction of the viscosity limiter (eq. 2.17) makes the predicted wall shear stress in better agreement with experimental data of separated flow. This feature also takes into consideration the transport mechanism of the turbulent shear stresses.

2.2.4 Langtry-Menter $k-\omega$ Shear Stress Transport model (SSTLM)

This model is a correlation-based transition model, built strictly on local variables from a combination between the strain-rate Reynolds number with experimental transition correlations using standard transport equations, according to Menter et al. (2006).

This model was developed for laminar-turbulent transition applications. It encompasses one transport equation for the intermittency γ (eq. 2.24), which can be used to trigger transition locally. Furthermore, it uses a transport equation for a transition onset momentum-thickness Reynolds number (eq. 2.25), required to capture the local influence of the turbulence intensity. These equations do not attempt to model the physics of the transition process, instead their aim is the implementation of transition correlations into general-purpose CFD methods.

$$\rho\frac{\partial\gamma}{\partial t}+\rho\bar{u}_j\frac{\partial\gamma}{\partial x_j}=P_{\gamma1}-E_{\gamma1}+P_{\gamma2}-E_{\gamma2}+\frac{\partial}{\partial x_j}\left[\left(\mu+\frac{\mu_t}{\sigma_\gamma}\right)\frac{\partial\gamma}{\partial x_j}\right] \tag{2.24}$$

$$\rho\frac{\partial(\tilde{R}e_{\theta t})}{\partial t}+\rho\bar{u}_j\frac{\partial\tilde{R}e_{\theta t}}{\partial x_j}=P_{\theta t}+\frac{\partial}{\partial x_j}\left[\sigma_{\theta t}(\mu+\mu_t)\frac{\partial\tilde{R}e_{\theta t}}{\partial x_j}\right] \tag{2.25}$$

Using the vorticity Reynolds number concept (equation 2.26) a link is provided between the transition onset Reynolds number from an empirical correlation and the local boundary-layer quantities.

$$Re_v=\frac{\rho y^2}{\mu}\left|\frac{\partial u}{\partial y}\right|=\frac{\rho y^2}{\mu}S, \qquad Re_\theta=\frac{max(Re_v)}{2.193} \tag{2.26}$$

An intricate set of relations containing the previous referred empirical correlations are described in the original article by Menter et al. (2006). As this falls out of the scope of this thesis, those correlations will not be presented here.

An important aspect is that this transition model interacts with the the $k-\omega$ SST turbulence model through:

$$\rho\frac{\partial k}{\partial t}+\rho\bar{u}_j\frac{\partial k}{\partial x_j}=\tilde{P}_k-\tilde{D}_k+\frac{\partial}{\partial x_j}\left[(\mu+\sigma_k\mu_T)\frac{\partial k}{\partial x_j}\right] \tag{2.27}$$

where:

$$\tilde{P}_k=\gamma_{eff}P_k; \qquad \tilde{D}_k=min(max(\gamma_{eff},0.1),1.0)D_k \tag{2.28}$$

$$R_y=\frac{\rho y\sqrt{k}}{\mu}, \qquad F_3=e^{-\left(\frac{R_y}{120}\right)^8}, \qquad F_1=max(F_{1,orig},F_3) \tag{2.29}$$

where P_k and D_k are the production and dissipation terms of turbulent kinetic energy of the $k-\omega$ SST model. The blending function F_1 is determined from the set of equations (2.29), where $F_{1,orig}$ is the original SST blending function.

In this way, this is a four equations eddy viscosity model, but where the eddy viscosity relation is as in the original SST (eq. 2.17).

Current limitations of the model are that crossflow instabilities or wall roughness are not present in the correlations used.

2.2.5 Realizable $k-\varepsilon$ model

This model was created to achieve a simpler more robust form of the dissipation rate equation than its standard formulation. Its transport equation for the dissipation rate ε is based on the dynamic equation for fluctuating vorticity. Besides, it also adopts a new realizable eddy viscosity formulation (eq. 2.30).

$$\nu_t=C_\mu\frac{k^2}{\varepsilon}, \qquad C_\mu=\frac{1}{A_0+A_SU^*\frac{k}{\varepsilon}} \tag{2.30}$$

Developing a model equation for the dynamic equation of the mean-square vorticity fluctuation $\overline{\omega_i\omega_i}$ and using relation (2.31), the transport equation for ε was obtained (eq. 2.32).

$$\varepsilon=\nu\overline{\omega_i\omega_i} \tag{2.31}$$

$$\frac{D}{Dt}(\rho\varepsilon)=\nabla(\rho D_\varepsilon+\nabla\varepsilon)+C_1\rho|S|\varepsilon-C_2\rho\frac{\varepsilon^2}{k+(\nu\varepsilon)^{0.5}} \tag{2.32}$$

The turbulence kinetic energy equation is given by equation (2.33) whereas the turbulence viscosity is given by equation (2.30).

$$\rho \frac{Dk}{Dt} = \nabla(\rho D_k \nabla k) + \rho G - \frac{2}{3}\rho(\nabla u)k - \rho\varepsilon \tag{2.33}$$

Furthermore, it gives improved predictions for the spreading rate of jets and a superior ability to capture the mean flow of complex structures and flows involving rotation and boundary layers under strong adverse pressure gradients, separation and recirculation, according to Shih et al. (1995). According to the original publication this model performs better than the standard $k-\varepsilon$ model in almost every tested case.

A common criticism that crosses all eddy-viscosity turbulence models is their incapability of accurately describing the subtle connection between turbulent energy production and turbulent stresses caused by anisotropy of the normal stresses (Versteeg and Malalasekera, 2007). The Reynolds stress models incorporate these effects.

2.3 Wall Funtions

The good performance of standard turbulence closure models in wall-bounded shear flows depend, to a large extent, upon the application of wall functions.

A wall function bridges the complete near wall zone and the flow region dominated by Reynolds stresses and characterized by a turbulent condition. They give the values for U_i, $\overline{u_i u_j}$, k and ε for the first grid point, located in the fully turbulent region. These functions avoid modelling the direct influence of a surface wall upon the eddy viscosity. The validity of this procedure is restricted to situations where either the Reynolds number is high enough for the viscous effects to be negligible or the wall function is well established, according to Patel et al. (1984).

$$y^+ = \frac{y u_\tau}{\nu} \tag{2.34}$$

The near wall region can be divided into three regions: the viscous sub-layer ($y^+ < 5$), the log-law region ($y^+ > 30$) and the buffer layer ($5 <= y^+ <= 30$).

Important properties for near-wall analysis are the friction velocity (u_τ) and the non-dimensional velocity (u^+) (shown in equation 2.35).

$$u^+ = \frac{U}{u_\tau}, \qquad u_\tau = \sqrt{\frac{\tau_w}{\rho}} \tag{2.35}$$

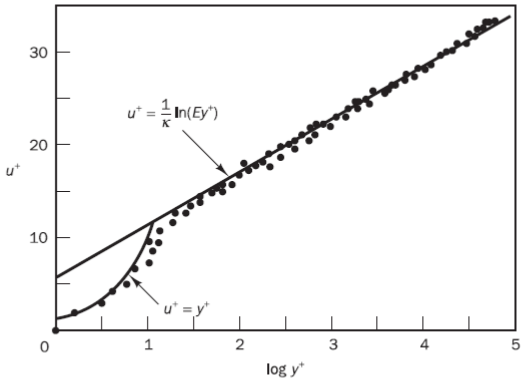

Figure 2.1: Viscous sub-layer and log-law region (taken form Versteeg and Malalasekera (2007))

Linear or viscous sub-layer

This is the closest region to the wall, dominated by viscous effects. The velocity profile is given by equation (2.36).

$$u^+ = y^+ \tag{2.36}$$

Log-law region

Outside the viscous sub-layer where the molecular stress is negligible, but sufficiently close so that the prevailing shear stress is essentially identical to the wall shear stress, we have the log-law region given by:

$$u^+ = \frac{1}{\kappa} ln(Ey^+) + B, \qquad \kappa = 0.41, \qquad E = 9.0 \tag{2.37}$$

Assuming that the first grid point is located in this specific log-law region, the flow properties (u, k and ε) in that point are calculated by the following set of equations:

$$u_c = \frac{u_\tau}{\kappa}\ln(y^+E), \qquad k_c = \frac{u_\tau^2}{\sqrt{c_\mu}}, \qquad \varepsilon_c = \frac{u_\tau^3}{\kappa y_c} \tag{2.38}$$

2.3.1 Wall functions in OpenFOAM

In real computation, there will be locations where the first node is not situated in the log law region and the code needs to function properly by imposing, instead, a corrected wall function that does not change the true physics of the flow. Since, as will be explained later we will be using the OpenFoam code, below we present the wall functions at our disposal in this code.

OpenFOAM has in its code some built in wall functions for various turbulence properties.

kqRWallFunction

Used as a boundary condition for the turbulent kinetic energy and it functions as the Neumann boundary providing a pure zero-gradient boundary condition.

This wall function is applied in regions with high y^+ (around 30). This way, the initial value of the turbulent kinetic energy in the first grid point is the same as the value of k in the inlet flow. The initial conditions are treated further in this text.

epsilonWallFunction

This boundary condition calculates ε on the cell centre through equation (2.39).

$$\varepsilon = \frac{1}{W} \sum_{f=i}^{W} \left(\frac{c_\mu^{3/4} k^{3/2}}{k y_i} \right) \tag{2.39}$$

where W is the weight of the cell, defined by how many faces of one cell use this boundary condition. k is turbulent kinetic energy at the cell center and y_i is the distance from the cell center to the wall, according to Liu (2016). The subscript f represents each face of the cell that use this boundary condition.

omegaWallFunction

The ω wall function provides the constraint on turbulence specific dissipation (ω). This wall function can switch between viscous and logarithmic region according to position of y^+. In the viscous layer, equation (2.40) is applied whereas in the logarithmic region equation (2.41) is used (Liu, 2016).

$$\omega_{visc} = \frac{6.0\nu}{\beta_1 y^2}, \qquad \beta_1 = 0.075 \tag{2.40}$$

$$\omega_{log} = \frac{k^{1/2}}{C_\mu^{1/4} k y} \tag{2.41}$$

nutkWallFuntion

This function gives the boundary condition for the turbulent viscosity near a surface wall. When y^+ is situated in the viscous sublayer region, this function imposes $\nu_t = 0$. In other situations it applies equation (2.42).

$$\nu_t = \nu \left(\frac{k y^+}{ln(E y^+)} - 1 \right) \tag{2.42}$$

2.4 Reynolds Stress models

The Reynolds stress models abandon the hypothesis of isotropic turbulence and isotropic eddy-viscosity by solving six transport equation for the Reynolds stresses, together with an equation for the dissipation rate.

Reynolds stress models predict the anisotropy of turbulent intensities, the curvature effect and the secondary motion better than the isotropic eddy viscosity model, according to Lee et al.

(2000). The transport equation for ε is shown in equation (2.43) and the set of six governing equations governing $-\overline{u_i u_j}$ is presented in equation (2.44).

$$\frac{D\varepsilon}{Dt} = \underbrace{c_\varepsilon \frac{\partial}{\partial x_k}\left(\frac{k}{\varepsilon}\overline{u_k u_l}\frac{\partial \varepsilon}{\partial x_l}\right)}_{diffusive\ transport} - \underbrace{\varepsilon_1 \frac{\varepsilon\overline{u_i u_k}}{k}\frac{\partial \bar{u}_i}{\partial x_k} - c_{\varepsilon 2}\frac{\varepsilon^2}{k}}_{net\ generation\ of\ \varepsilon} \tag{2.43}$$

$$\frac{\partial \overline{u'_i u'_j}}{\partial t} + \bar{u}_k \frac{\partial}{\partial x_k}(\overline{u'_i u'_j}) = P_{ij} + d_{ij} + \phi_{ij} - \varepsilon_{ij} + \frac{\partial}{\partial x_k}\left(\nu \frac{\partial \overline{u'_i u'_j}}{\partial x_k}\right) \tag{2.44}$$

P_{ij} is the production term (eq. 2.45), d_{ij} is the turbulent diffusion term (eq. 2.46), ϕ_{ij} is the pressure-strain redistribution term, and ε_{ij} is the dissipation term (eq. 2.47).

$$P_{ij} = -\left[\overline{u'_j u'_k}\frac{\partial \bar{u}_j}{\partial x_k} + \overline{u'_j u'_k}\frac{\partial \bar{u}_i}{\partial x_k}\right] \tag{2.45}$$

$$d_{ij} = \frac{\partial}{\partial x_k}\left[\frac{c_\mu}{k}\frac{k^2}{\varepsilon}\frac{\partial \overline{u'_i u'_j}}{\partial x_k}\right] \tag{2.46}$$

$$\varepsilon_{ij} = \frac{2}{3}\delta_{ij}\varepsilon \tag{2.47}$$

The most important quantity to be modelled is the pressure-rate-of-strain tensor, also called pressure-strain. In Reynolds-stress models, ϕ_{ij} is modelled as a local function of $\overline{u'_i u'_j}$, ε and $\frac{\partial \bar{u}_i}{\partial x_j}$ according to Pope (2000). The difference between many existing Reynolds stress models lies precisely in the treatment they give to the pressure-strain term (ϕ_{ij}).

There are three qualitatively different contributions to ϕ_{ij}. The rapid pressure $\phi_{ij,1}$, involving mean velocity gradients, the slow tensor $\phi_{ij,2}$, which can be expected to be significant in most circumstances, and the harmonic component which is only important near walls (Pope, 2000).

2.4.1 Launder-Reece-Rodi (LRR) model

Equation (2.48) defines the Reynolds stress anisotropy tensor b_{ij}.

$$a_{ij} = \overline{u'_i u'_j} - \frac{2}{3}k\delta_{ij}; \quad b_{ij} = \frac{a_{ij}}{2k} \tag{2.48}$$

Starting with the work of Launder *et al.* (1975), anisotropic models for the rapid pressure strain correlation have been formulated where the coefficients of the mean velocity gradients are taken to be functions of the anisotropy tensor b_{ij} (eq. 2.49).

$$\phi_{ij,1} = -c_1 \varepsilon b_{ij} \tag{2.49}$$

$$\phi_{ij,2} = c2\left[\overline{u'_j u'_l}\frac{\partial \bar{u}_i}{\partial x_l} + \overline{u'_i u'_l}\frac{\partial \bar{u}_j}{\partial x_l} - \frac{1}{3}\delta_{ij}\overline{u'_l u'_m}\frac{\partial \bar{u}_l}{\partial x_m}\right] \tag{2.50}$$

The approximation adopted to the pressure-strain correlations appear to give reasonably satisfactory partitioning of the stresses both near walls and in free shear flows. Table (2.5) presents the coefficients of this model.

Table 2.5: Coefficients in the LRR model

c_1	c_2	c_{w1}	c_{w2}
1.8	0.6	0.5	0.3

2.4.2 Speziale-Sarkar-Gatski (SSG) model

For the SSG model, the pressure-strain correlation has been modelled based on invariance arguments and a dynamical systems approach. The rapid pressure-strain is given by:

$$\phi_{ij,1} = -\left(c_1\varepsilon + c_1^* P\right) b_{ij} + c_2\varepsilon\left(b_{ik}b_{kj} - \frac{1}{3}b_{mn}b_{mn}\delta_{ij}\right) \tag{2.51}$$

and its slow counterpart is defined by:

$$\phi_{ij,2} = \left(c_3 - c_3^*\Pi^{0.5}\right) K\overline{S}_{ij} - c_4 K\left(b_{ik}\overline{S}_{jk} + b_{jk}\overline{S}_{ik}\right) - \frac{2}{3}b_{mn}\overline{S}_{mn}\delta_{ij} - c_5 K\left(b_{ik} + W_{jk} + b_{jk}Wik\right) \tag{2.52}$$

where the mean rate of strain tensor $\overline{S}_{ij}$, is defined by:

$$\overline{S}_{ij} = \frac{1}{2}\left(\frac{\partial \overline{u}_i}{\partial x_j} + \frac{\partial \overline{u}_j}{\partial x_i}\right) \tag{2.53}$$

Table 2.6: Coefficients in the SSG model

$\overline{C}_1$	C_1'	C_1	c_1^*	c_2	c_3	c_3^*	c_4	c_5
$7.5A^{0.5}A_2$	0.6	3.8	1.8	4.2	0.8	1.3	1.25	0.4

The SSG model appears to yield improved results over the LRR model for homogeneous turbulent flows which include plane strain, rotating plane shear, and the axisymmetric expansion/contraction, according to Speziale et al. (2000). However, this new approach did not solve some previous deficiencies like the description of rotating turbulent shear flows. These deficiencies are intrinsic to the general hierarchy of pressure-strain models and cannot be eliminated by the addition of more complex nonlinear terms as explained by Speziale et al. (2000).

2.5 Low Reynolds Number models

The turbulence models previously shown require wall functions to bridge the gap between the wall and the first computational node, assuming that in this gap there is a "well-behaved" (standard) boundary layer. In flows around bluff bodies this is often not the case. Low Reynolds turbulence models on the other hand resolve that region that all the way to the surface wall, encompasses also the viscous sub-layer. In this way no wall functions are employed.

These models were developed for flows at moderate Reynolds numbers. They require a high grid resolution near the wall so as to give an y^+ value of at least 1 along the grid line closest to the wall, according to Jaw (1998). This is mainly due to the steep gradients that the velocity and ε have in this region.

Most low Reynolds models contain an *ad hoc* damping function f_μ in the eddy-viscosity expression to account for the effect of wall proximity in strongly dampening the Reynolds stresses. This function corrects the improper asymptotic behavior of the eddy-viscosity formulation when approaching a solid wall. The damping function is often non-linear and causes numerical stiffness, according to Lien and Kalitzin (2001). Furthermore, damping functions are often applied in the some terms within the transport equations as well. Besides that, in wall vicinities the effects of molecular diffusion also need to be taken into account.

2.5.1 Linear $k-\varepsilon$ models

These models apply a damping formulation for the linear eddy viscosity closure that is generally written as in equation (2.54).

$$\nu_t = C_\mu f_\mu \frac{k^2}{\varepsilon} \tag{2.54}$$

Hence, they still rely on a transport equation for k (eq. 2.55) and another one for ε (eq. 2.56).

$$\frac{\partial}{\partial t}(\rho k) + \frac{\partial}{\partial x_j}\left[\rho k u_j - \left(\mu + \frac{\mu_t}{\sigma_k}\right)\frac{\partial k}{\partial x_j}\right] = P - \rho\varepsilon - \rho D \tag{2.55}$$

$$\frac{\partial}{\partial t}(\rho \varepsilon) + \frac{\partial}{\partial x_j}\left[\rho \varepsilon u_j - (\mu + \frac{\mu_t}{\sigma_\varepsilon})\frac{\partial \varepsilon}{\partial x_j}\right] = (C_{\varepsilon 1} f_1 P - C_{\varepsilon 2} f_2 \rho \varepsilon)\frac{\varepsilon}{k} + \rho E \tag{2.56}$$

$$P = -\overline{u_i u_j}\frac{\partial u_i}{\partial x_j} \tag{2.57}$$

Table (2.7) presents the coefficients corresponding to the turbulence models of Lien and Leschziner, Launder-Sharma $k-\varepsilon$ and Lam-Bremhorst $k-\varepsilon$.

For the Lien and Leschziner model there is an extra correlation:

$$P_k' = \frac{C_{\varepsilon 2} k^{3/2}}{3.53 l_n \left[1 - e^{(-0.263 l_n^*)}\right]} e^{[-0.00222 l_n^{*2}]} \tag{2.58}$$

These models have been found to perform rather poorly in boundary layer with adverse pressure gradient (Jaw, 1998).

Table 2.7: Coefficients for the $k-\varepsilon$ turbulence models

	Lien Leschziner	Launder-Sharma	Lam-Bremhorst
c_μ	$0.09\left[\frac{1-e^{-0.016 l_n^*}}{1-e^{-0.263 l_n^*}}\right]$	0.09	0.09
σ_k	1	1	1
σ_ε	1.3	1.3	1.3
D	0	$2\nu\left(\frac{\partial\sqrt{k}}{\partial y}\right)^2$	0
E	0	$2\nu\nu_t\left(\frac{\partial^2 u}{\partial y^2}\right)^2$	0
ε_{wall}	0	0	$\nu\frac{\partial^2 k}{\partial y^2}$
$C_{\varepsilon 1}$	$1.44\left(1+\frac{P_k'}{P}\right)$	1.44	1.44
$C_{\varepsilon 2}$	$1.92\left(1-0.3e^{-R_T^2}\right)$	1.92	1.92
f_μ	1	$e^{\frac{-3.4}{(1+R_t/50)^2}}$	$\left[1-e^{(-0.0165R_y)^2}\right]\left(1+\frac{20.5}{R_T}\right)$
f_1	1	1	$1+\left(\frac{0.05}{f_\mu}\right)^3$
f_2	1	$1-0.3e^{-Re_t^2}$	$1-e^{-R_T^2}$

2.5.2 $\overline{v^2}-f$ model

The $\overline{v^2}-f$ model shows very good performance in several test cases with separated flows at low speeds. The development of this model was inspired by second moment closure, necessary for a satisfactory recirculation prediction. The eddy viscosity is given by equation (2.59), where the scalar $\overline{v^2}$ is akin to wall normal Reynolds stress. This quantity is obtained from a transport equation simplified from second-moment closure (eq. 2.60).

The introduction of $\overline{v^2}$ allows to consider the stronger effects of turbulence dampening in directions normal to walls into the eddy viscosity calculation.

The term kf in equation (2.60) plays the role of pressure strain, which is responsible for the redistribution of turbulence energy from the streamwise component (Lien and Kalitzin, 2001), i.e., here it plays a role of turbulence production.

The anisotropic wall effects are modelled through the elliptic relaxation function f (eq. 2.61).

$$\nu_t = C_\mu \overline{v'^2} T \tag{2.59}$$

$$\frac{\partial \overline{v'^2}}{\partial t} + u_j \frac{\partial \overline{v'^2}}{\partial x_j} = kf - \overline{v'^2}\frac{\varepsilon}{k} + \frac{\partial}{\partial x_j}\left[\left(\nu + \frac{\nu_t}{\sigma_\varepsilon}\right)\frac{\partial \overline{v'^2}}{\partial x_j}\right] \tag{2.60}$$

$$L^2 \frac{\partial^2 f}{\partial x_j^2} - f = \frac{1}{T}(C_1 - 1)\left[\frac{\overline{v'^2}}{k} - \frac{2}{3}\right] - C_2 \frac{P_k}{k} \tag{2.61}$$

$$kf = \phi_{22} - \varepsilon_{22} + \frac{\overline{v'^2}}{k}\varepsilon, \quad \phi_{22} = -2\frac{\overline{v'^2}}{k}\varepsilon, \quad \varepsilon_{22} = 4\frac{\overline{v'^2}}{k}\varepsilon \tag{2.62}$$

$$T = min\left[max\left[\frac{k}{\varepsilon}, 6\sqrt{\frac{\nu}{\varepsilon}}\right], \frac{0.6k}{\sqrt{6}C_\mu \overline{v^2} S}\right] \tag{2.63}$$

$$L = C_L max\left[min\left[\frac{k^{3/2}}{\varepsilon}, \frac{k^{3/2}}{\sqrt{6}C_\mu \overline{v^2} S}\right], C_\eta \frac{\nu^{3/4}}{\varepsilon^{1/4}}\right] \tag{2.64}$$

2.5.3 Lien Cubic $k-\varepsilon$ model

Every model presented so far was based on the Boussinesq assumption (equation 2.4). For the low Reynolds Lien Cubic model however, the closure relation has an higher order correlation (equation 2.66). It is in fact a non linear $k-\varepsilon$ model.

$$\nu_T = C_\mu f_\mu \frac{k^2}{\varepsilon} \tag{2.65}$$

$$\begin{aligned}\frac{\overline{u'_i u'_j}}{k} = \frac{2}{3}\delta_{ij} - \frac{\nu_T}{k}S_{ij} + C_1 \frac{\nu_T}{\varepsilon}\left[S_{ik}S_{kj} - \frac{1}{3}\delta_{ij}S_{kl}S_{kl}\right] + C_2 \frac{\nu_T}{\varepsilon}\left[\Omega_{ik}S_{kj} + \Omega_{jk}S_{ki}\right] + \\ + C_3 \frac{\nu_T}{\varepsilon}\left[\Omega_{ik}\Omega_{jk} - \frac{1}{3}\delta_{ij}\Omega_{kl}\Omega_{kl}\right] + HOT\end{aligned} \tag{2.66}$$

$$HOT = C_4 \frac{\nu_T k}{\varepsilon^2}\left(S_{ki}\Omega_{lj} + S_{kj}\Omega_{li}\right)S_{kl} + C_5 \frac{\nu_T k}{\varepsilon^2}\left(S_{kl}S_{kl} - \Omega_{kl}\Omega_{kl}\right)S_{ij} \tag{2.67}$$

where the coefficients and dampening functions are given by the following set of equations.

$$C_\mu = \left.\frac{0.667}{A_1 + S + 0.9\omega}\right|_{A_1 = 1.25} \tag{2.68}$$

$$f_\mu = \left[1 - e^{-0.0198 y^*}\right]\left(1 + \frac{5.29}{y^*}\right), \quad y^* = y\frac{\sqrt{k}}{\nu} \tag{2.69}$$

$$C_1 = \frac{3/4}{(1000 + S^3)}, \quad C_2 = \frac{15/4}{(1000 + S^3)}, \quad C_3 = \frac{19/4}{(1000 + S^3)} \tag{2.70}$$

$$C_4 = -10C_\mu^2, \quad C_5 = -2C_\mu^2 \tag{2.71}$$

Through equation (2.66), this model no longer assumes Reynolds stress isotropy even though it continues to apply the eddy viscosity concept. The inclusion of non-linear terms precisely allows turbulence anisotropy to be predicted. This model mimics the sensitivity to streamline curvature in simple flows but does not present the associated physical mechanism in a correct manner, according to Lien et al. (1996).

Another criticism is that it enhances the turbulence level in stagnation regions. Besides, in complex flows it doesn't return an adequate interaction between turbulence and streamline curvature across the whole flow domain.

Chapter 3

Solvers and Numerical Schemes

The software used for the CFD simulations was *OpenFOAM* version 1712, a software developed by CFD Direct and OpenCFD Ltd. It is an open source software programmed in C++. The overall structure of a CFD code is constituted by three individual building blocks: the pre-processor, the solver and the post-processor. A quick overview on the user interface of *OpenFOAM* is given in annex A.

3.1 Pre-processor

This step consists on the input of a flow problem to a CFD simulation. The operator defines the problem geometry and computational domain, selects the physical and chemical phenomena to be modelled, fluid properties and boundary conditions.

Both the accuracy of a solution and its computational cost are dependent on the refinement of the chosen grid (Versteeg and Malalasekera, 2007), on the order of discretization and interpolation schemes used to build the algebraic equations from the differential equations.

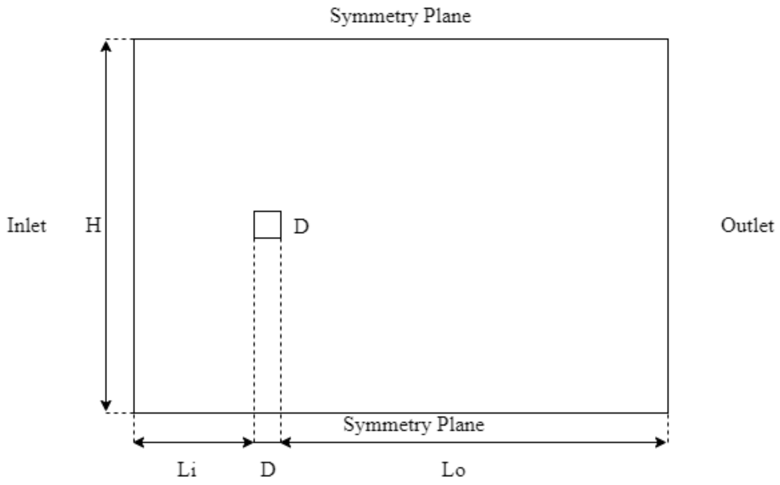

Figure 3.1: Problem geometry of our simulations

Our turbulent flow simulation around a two-dimensional square cylinder will be carried out for $Re = 21400$ around a square cylinder. In figure 3.1 our geometry is shown schematically. The left boundary is the inlet plane, where our flow enters the domain with the appropriate velocity. The right boundary is the outlet region, where the flow leaves the domain. The outlet boundary is sufficiently far from the cylinder that the flow is already parallel and essentially a condition of null streamwise gradient can be imposed for all quantities that it does not affect the flow in the vicinity of the cylinder.

The square cylinder has a side length D. The remaining dimensions will be shown in each simulation since they are not the same in every setup. The cylinder is considered to be very long, so that in the spanwise direction we consider symmetry boundary conditions to allow for 2D computations in the laminar and turbulent flow RANS calculations. The boundary conditions shown in table (3.1) for the domain inlet, outlet, upper/lower and front/bottom planes are the same for every simulation. The wall functions applied at the cylinder walls change with the simulation. The specifics of each simulation will be mentioned for each case.

Table 3.1: Boundary conditions used in every simulation

Boundary	U	p
Front/Bottom plane	Empty	Empty
Upper/Lower plane	Symmetry plane	Symmetry plane
Inlet	Fixed horizontal velocity (U,0,0)	Zero gradient condition
Outlet	Zero gradient condition	Fixed value of 0
Cylinder Walls	No Slip (U=0)	Zero Gradient ($\frac{\partial p}{\partial y} = 0$)

3.2 Numerical Method

The solver consists on the algorithm chosen to achieve the numerical solution of the algebraic equations. It includes the discretisation and integration of the governing equations over all control volumes of the domain and the iterative method adopted to reach the numerical solution. These can be found in such textbooks as Versteeg and Malalasekera (2007). They are not described in length here since the aim of this thesis was not the development of numerical methods, we used available tools. Nevertheless a very brief overview is given below.

As mentioned before, the equations that describe our physical problem are the continuity equation (2.3), the Reynolds equations (2.2) and the turbulence model equations. However, as it was shown throughout section 2, even though the governing equations used depend on the turbulence model adopted they can all be written in a general form as below

$$\frac{\partial \phi}{\partial t} + \bar{u}_j \frac{\partial \phi}{\partial x_j} = P_\phi - D_\phi + S_\phi \tag{3.1}$$

where P_ϕ is the production term, D_ϕ the diffusion term and S_ϕ term representing the sources.

The governing equations are first volume-integred an operation that benefits, in some of its terms, from the application of Gauss theroem, given in equation (3.2).

$$\int_{CV} div(a)dV = \int_{A} n \cdot adA \tag{3.2}$$

The ensuing equation is then discretized using adequate hypothesis and levels of approximation. In openfoam, the discretization schemes are defined in the script *fvSchemes*. Table (3.2) shows every scheme used in this project.

Table 3.2: Numerical schemes used for this project

Time schemes	Steady-state; Backward
Gradient Schemes	Gauss linear
Divergence Schemes	QUICK; Linear upwind; Upwind
Interpolation Schemes	Linear

3.2.1 Discretization Schemes

Interpolation Schemes

First order upwind

This is a first-order bounded, very stable scheme. The lack of accuracy when compared to other schemes is its main setback. It is used mainly when the Peclet number is bigger than 2.

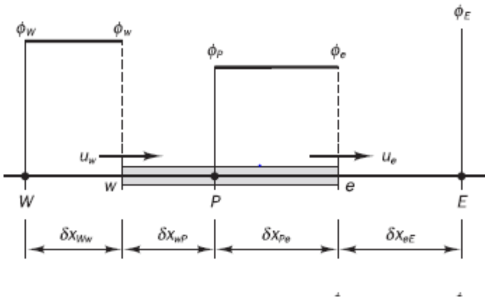

Figure 3.2: Illustrative scheme to understand upwind scheme (taken from (Versteeg and Malalasekera, 2007)

When the flow is in the positive direction, with $u_w > 0$ and $u_e > 0$ (according to figure 3.2), this scheme returns equation (3.3) for the east face value ϕ_e. This interpolation scheme produces erroneous results when the flow is not aligned with the grid lines. It is too inaccurate to be considered as the first discretization option for our simulations. However, because of some stability problems using higher order schemes for some of the low Reynolds number simulations, this scheme was used as a last resource to obtain a solution. That said, we should keep in mind the lack of accuracy of the solutions attained, something that is discussed further in this thesis.

$$\phi_e = \phi_p \tag{3.3}$$

Linear Upwind

The linear upwind is a second-order extension of the upwind scheme. According to figure 3.2, considering a flow with positive direction ($u_w > 0$ and $u_e > 0$), it yields the following expression for ϕ_e:

$$\phi_e = \frac{3\phi_p - \phi_W}{2} \tag{3.4}$$

When the Peclet number is bigger than 2, the calculations tend to become unstable.

QUICK Scheme

The QUICK scheme is a second order, unbounded divergence scheme. According to figure 3.3 the value of ϕ_e is given by equation (3.5).

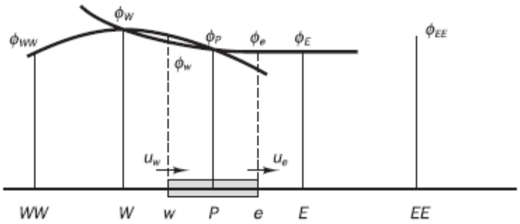

Figure 3.3: Quadratic profile used in QUICK scheme (taken from Versteeg and Malalasekera, 2007)

$$\phi_e = \frac{3}{8}\phi_E + \frac{6}{8}\phi_p - \frac{1}{8}\phi_W \tag{3.5}$$

Gauss Linear

Gauss linear is a laplacian scheme used in openFOAM as the discretization scheme for the diffusion term. This scheme is commonly known as central differencing scheme. According to figure 3.2, considering $u_w, u_e > 0$, the values of ϕ in the east and west cell faces are obtained through:

$$\phi_e = \frac{\phi_P + \phi_E}{2}, \qquad \phi_w = \frac{\phi_W + \phi_P}{2} \tag{3.6}$$

Time Schemes

Steady state

$$\frac{\partial}{\partial t}(\phi) = 0 \tag{3.7}$$

This scheme sets the temporal contributions to zero. This way, each time step of the simulation does not correspond to a physical time but rather to an iteration towards the steady state solution.

Backward Differencing Scheme

$$\frac{\partial}{\partial t}(\phi) = \frac{1}{\Delta t}\left(\frac{3}{2}\phi - 2\phi^{0} + \frac{1}{2}\phi^{00}\right) \tag{3.8}$$

This is a transient, second order implicit, potentially unbounded and conditionally stable numerical scheme.

3.2.2 Algorithm

SimpleFoam

SimpleFoam is an openFOAM solver that uses the SIMPLE (Semi-Implicit Method for Pressure-Linked Equations) algorithm, for incompressible, steady flow. Since it is a steady state solver, each new iteration is new step towards the numerical solution, not corresponding to a physical time. The algorithm is shown in the flow chart of figure 3.4.

In our simulations, the calculated solution was said to have reached steady state when the residuals evolution stopped decreasing and their magnitude was in the order of 10^{-3}.

PisoFoam

PisoFoam is an incompressible, transient openFOAM solver that uses the PISO (Pressure Implicit with Splitting of Operators) algorithm.

The PISO algorithm is an extent of the SIMPLE algorithm to solve the Navier-Stokes equations. It involves one predictor step and two corrector steps and is designed to satisfy mass conservation (Versteeg and Malalasekera, 2007). Until the correct pressure and velocities are attained, this algorithm is the same as the SIMPLE algorithm. The algorithm steps are shown in figure 3.5.

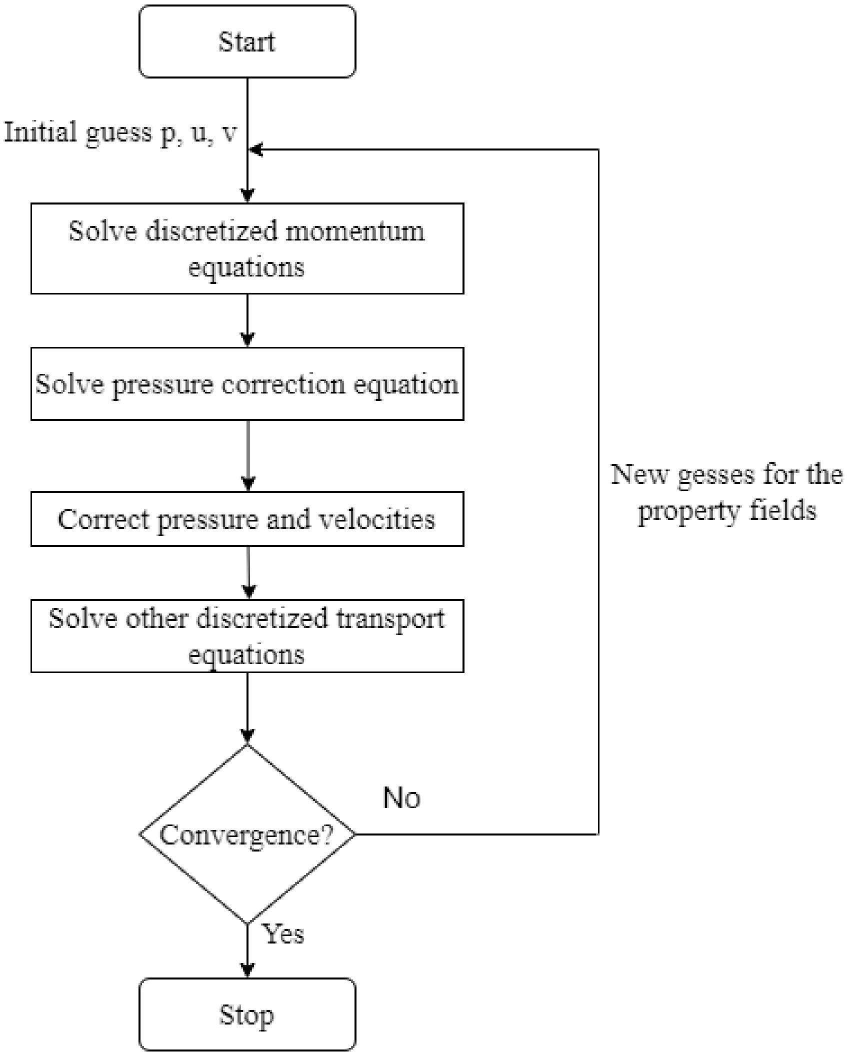

Figure 3.4: The SIMPLE algorithm

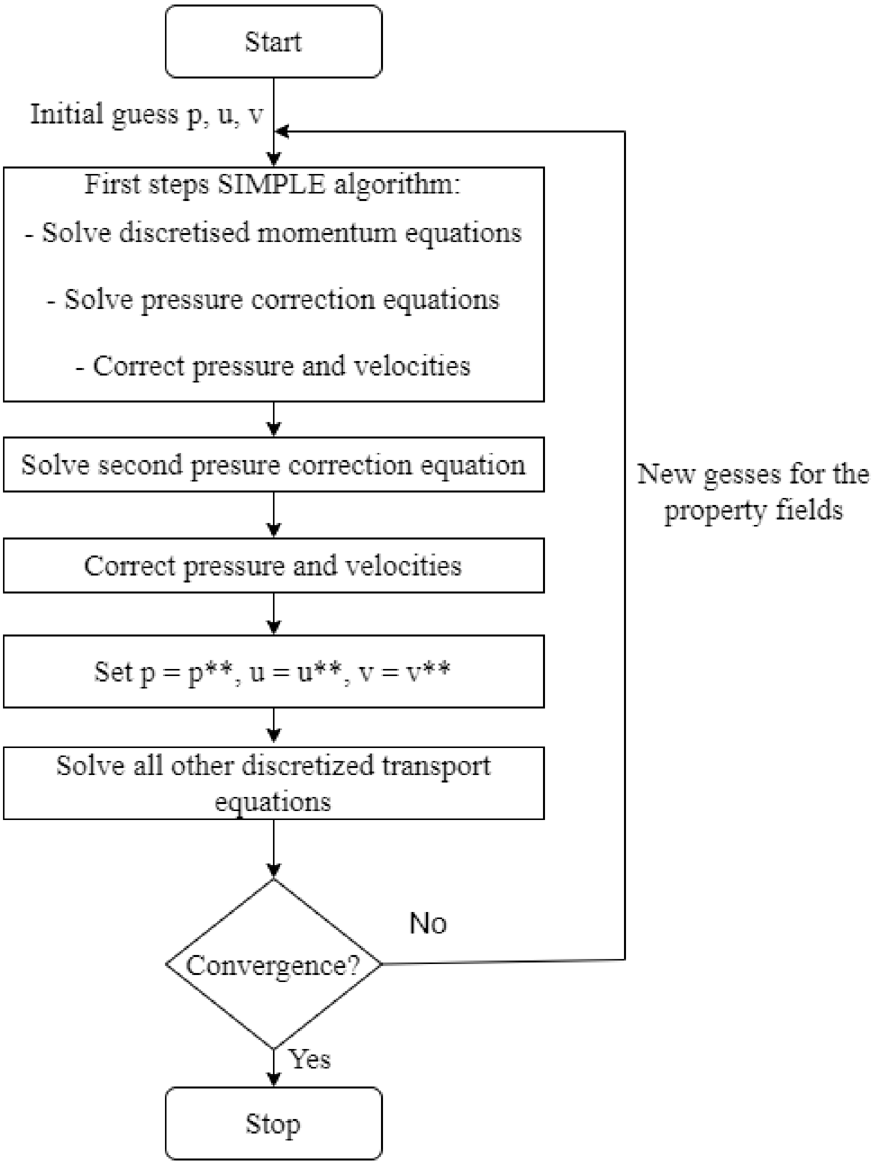

Figure 3.5: The PISO algorithm

Chapter 4

Results and Discussion

This section presents the significant results obtained during the project. First the results obtained for the laminar simulations will be presented. These simulations were carried out for various reasons. On one hand the results for $Re = 10$ were used to make a sensitivity test of the mesh, to establish its adequacy for the execution of the simulations. Furthermore, the simulations were employed to measure the accuracy of the mesh and methods employed. The $Re = 100$ case was especially important as an assessment if the established setup was able to capture the expected unsteady behaviour, characteristic of this flow. Following that, the results for the turbulent flow simulations around a square cylinder are presented and discussed. All the turbulence models discussed in section 2 were used in the simulations.

The turbulent flow has a Reynolds number $(U.D/\nu)$ of 21400 and the characteristic length of the cylinder $D = 0.1\ m$. The flow enters the domain horizontally with an inlet velocity $U = 0.214\ m/s$ with artificially induced turbulence intensity which was set to be of 2%. Tests were made to ensure the initial turbulence intensity defined did not have any impact on the results obtained.

The results presented are compared with published data to get a more accurate conclusion as to their validity. The comparisons will be carried out not only in terms of local quantities, like local velocities, but also in terms of global quantities like the drag coefficient or the Strouhal numbers. The drag coefficient in addition to the Strouhal number (eq. 4.1) based on the lift coefficients, are compared with experimental data. Furthermore, the velocity profiles and the streamline visualisation of the flow are also presented. Also, phase-averaged velocity profiles are shown for the various unsteady flows calculated.

The lift coefficient, the drag coefficient and the strouhal number are defined as:

$$C_L = \frac{F_L}{\frac{1}{2}\rho A U_o^2} \qquad C_D = \frac{F_D}{\frac{1}{2}\rho A U_o^2} \qquad St = \frac{f \cdot U}{L}, \tag{4.1}$$

where F_L is the lift force on the cylinder, F_D is the drag force on the direction of the flow and A is the projected frontal area of the cylinder.

The average C_L is 0 due to the oscillating nature of the lift coefficient in this flow. However, when the flow becomes time-dependent, the C_L becomes non-zero and time dependent.

The turbulent flow around a square cylinder has been the object of study for many investigators. It is a fully three dimensional, turbulent flow with flow separations along the side wall as well as vortex shedding features. The flow wake is characterized by coherent structures such as the Kelvin-Helmholtz instabilities within the separated shear layers and the Kármán vortex street in the near wake region. In each separated shear layer, at the top and bottom sides of the cylinder, the instabilities lead to a vortex sheet roll up that favours the multi-scales features of the flow, according to Minguez et al. (2011). The flow tends to separate at the upstream sharp edge of the square. The strong separation and adverse pressure gradients, the large scale eddying turbulence structures and unsteady processes make this flow very challenging for numerical modelling.

The simulations were performed in the *HPC cluster* of FEUP. The post processing work was carried out using *MatLab*® and *Paraview*® software.

4.1 Laminar Flow

Laminar flow simulations were performed for three different Reynolds number: 10, 40, 100. For Reynolds numbers 10 and 40, the results show steady flow with separation taking place at the rear of the cylinder. The contour and streamline plots (figs. 4.1 and 4.2) of the streamline velocity show the recirculation region and the smooth fluid layers around the cylinder, characteristic of this flow.

For $Re = 100$ the flow becomes unsteady with an unsteady oscillation in the wake region. As expected at low Re, the laminar oscillations were alternating around the axis. Figure 4.3 shows and instantaneous plof of the streamlines that illustrates well the vortex street in the wake region and the characteristic oscillation of this flow.

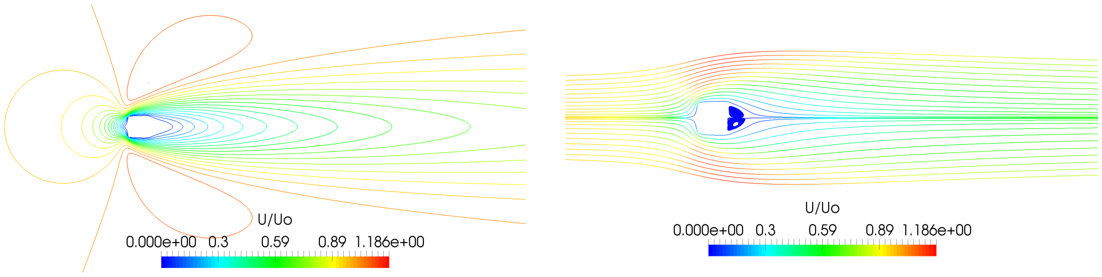

(a) (b)

Figure 4.1: Contours of the streamwise velocity component (4.1a) and streamlines (4.1b) for $Re = 10$. The colour code provides the magnitude of the normalised velocity.

To establish the adequacy of the mesh, we performed simulations for the flow at Re=10 using four meshes with different spatial resolutions. Each successive mesh was generated by making a global refinement such that the total number of nodes and elements increased by a factor of 2. Some conclusions regarding the mesh were drawn using Richardson's extrapolation method. For

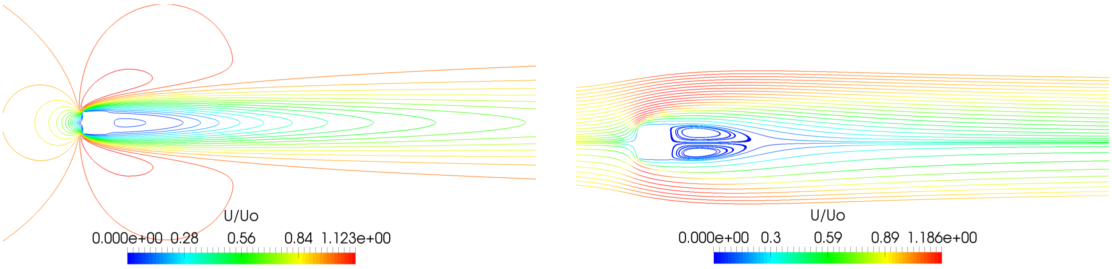

(a) (b)

Figure 4.2: Contours of the streamwise velocity component (4.2) and streamlines (4.2b) for $Re = 40$. The colour code provides the magnitude of the normalised velocity.

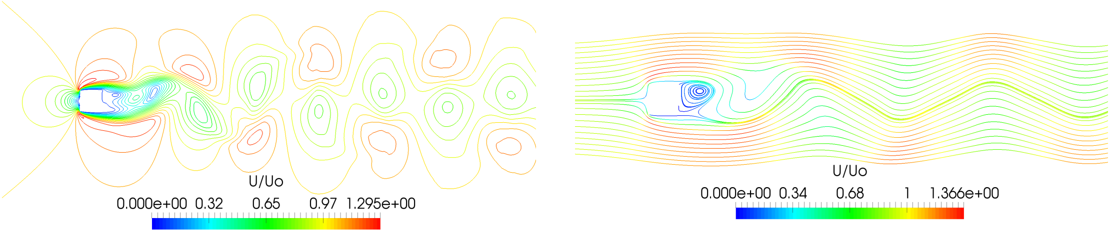

(a) (b)

Figure 4.3: Contours of the streamwise velocity component (4.3a) and streamlines (4.3b) for $Re = 100$. The colour code provides the magnitude of the normalised velocity.

Re = 40 and Re = 100, we used the most suitable mesh we got from the first four simulations. The solver used for cases Re=10 and Re=40 was simpleFoam whereas pisoFoam was used for the unsteady simulation.

4.1.1 Re=10 and Re=40

The computational domain size is $100D \times 40D$ distributed as per figure 3.1, into $L_1 = 29.5D$, $L_o = 69.5D$ and $H = 40D$. The blockage B of this setup is 0.025.

Mesh Convergence Study

As mentioned before, the simulations for $Re = 10$ were initially made using four meshes of different spatial refinement. Table 4.1 shows the number of cells in each mesh used, the number of cells around the cylinder face and the resultant drag coefficient. These results for C_d were used to make a mesh convergence study. Equation (4.2) shows that we achieved a first order of convergence. The theoretical order of convergence is 2. The difference might be related with the way the drag coefficient is calculated in openFOAM. In the software, the pressure and viscous forces acting on the cylinder surfaces are integrated in the direction of the flow (for the drag coefficient) and in the perpendicular direction (for the lift coefficient). Equations (4.1) are then applied to attain the coefficients. If the order of the method used by OpenFoam to calculate the force is lower that the order of methods used in the CFD simulation itself, then the order of convergence of the final result will be defined by the lowest order method.

Table 4.1: Mesh refinements used for the different meshes for $Re = 10$

Mesh	Number of cells	Cells around cylinder face	Cd
M1	22993	11	3.0871
M2	89954	21	3.1101
M3	361100	43	3.1209
M4	1439264	84	3.1259

$$p = \left| ln\left(\frac{3.1259 - 3.1209}{3.1209 - 3.1101}\right)/ln(2)\right| = 1.11 \tag{4.2}$$

Results

The results obtained (table 4.2) were compared with the numerical results from Sen et al. (2011). The predictions of the drag coefficient are in good agreement with those from the literature (within 1.7% for $Re = 10$ and 0.5% for $Re = 40$). The separation length on the other hand was a bit worse (within 3.8% for $Re = 10$ and 2.5% for $Re = 40$).

The separation length is referred to the separation zone existent at the rear of the cylinder. The resulting recirculation bubble is clear for both $Re = 10$ and $Re = 40$ in figures 4.1b and 4.2b, respectively.

Table 4.2: Comparison between the results obtained and the literature for $Re = 10$ and $Re = 40$

Re	C_d (Present)	C_d Sen et al. (2011)	l/D (Present)	l/D Sen et al. (2011)
10	3.1209	3.0700	0.6055	0.6295
40	1.6780	1.6697	2.7929	2.8638

4.1.2 Re=100

The simulation for $Re = 100$ was prepared according to the setup presented by Pantokratoras (2016). In this case, the domain has dimensions of $70D \times 20D$ in the streamwise and transverse directions and according to figure 3.1, $H = 20D$, $L_i = 19.5D$ and $L_o = 49.5D$. Emulating the benchmark setup, the boundary conditions for the upper and lower planes were changed from symmetry planes to moving walls with $U_x = 0.01$ *m/s*. The transient terms were discretized with the *backward* time scheme and *QUICK* interpolation scheme was used for advection.

The results obtained for the drag coefficient are presented in table 4.3 and shown to be within 2% of the literature data whereas the difference for the Strouhal is of the order of 6.5%.

Figure 4.4 compares the time variation of the drag coefficient showing that the magnitude of the periodic C_d computed is actually larger than that of the literature. Since excessive diffusion introduced by numerical schemes tend to reduce the amplitude this is a good sign if the quality of our simulations. The symmetric variation of C_d together with the variation of the recirculation length at the cylinder rear (fig. 4.6) are proof of the regular behaviour of the oscillating wake. Furthermore, the frequency spectrum (fig. 4.6) reiterates this idea showing a single peak in the frequency spectrum that characterizes the shedding process.

The time averaged transverse profiles of the streamwise velocity shown in figure 4.5 present the downstream evolution of the velocity profiles. The plotted lines display the velocity recovery along the cylinder wake. Five diameters downstream of the cylinder the profile is nearly recovered. Furthermore, this figure together with the phase averaged velocity profiles (fig. 4.7) confirm the foreseen symmetry on the mean flow around the cylinder axis. The different phases confirm that the flow reached an unsteady periodic behaviour. For a better understanding of those graphs (see figure 4.7 as an example) each graph represents a single phase with a different color, that has correspondence to the circular caption.

Table 4.3: Comparison between drag coefficient and Strouhal number

	Present	Pantokratoras (2016)
C_d	1.48	1.51
St	0.147	0.138
l/D	1.887	–

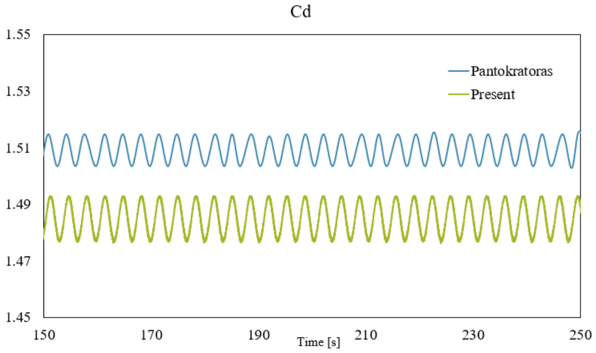

Figure 4.4: Comparison between the computed and reference data from literature of drag coefficient

4.2 Turbulent Flow

In this section, after an initial presentation on the geometry dimensions and initial conditions imposed onto the various properties required by the turbulence models, the main results are presented and properly discussed.

As for the laminar flow at Reynolds number of 100, the turbulent flow is unsteady, i.e., the Reynolds averaged characteristics depend on time, but many comparisons below are based on the average over the whole cycle of variation of the properties. If that has not a significant impact as far as an assessment of the mean flow is concerned (except that it removes the time dependency),

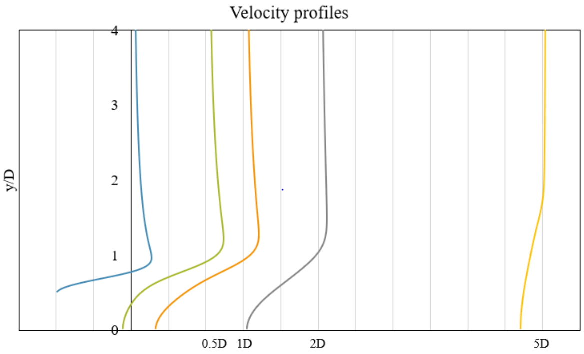

Figure 4.5: Averaged velocity profiles at various stations for $Re = 100$

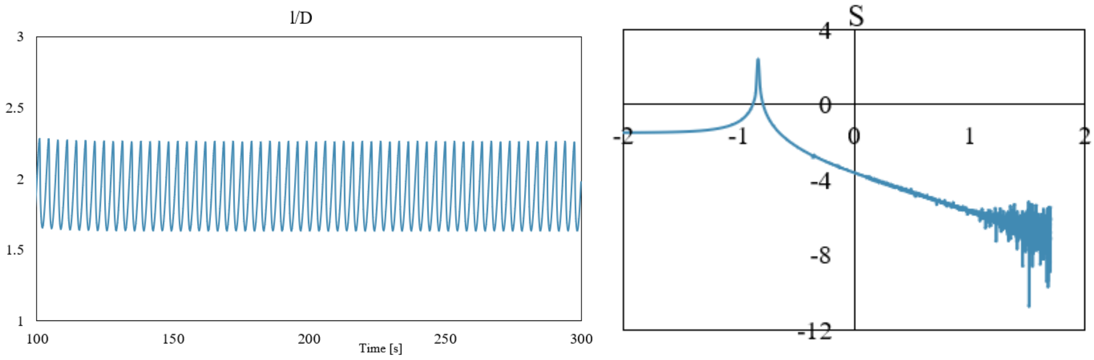

(a)

(b)

Figure 4.6: Separation length and frequency spectrum

it leads to an overestimation of the turbulent quantities, like the Reynolds stresses which become biased to higher values.

4.2.1 Case setup and boundary conditions

The domain dimensions for the turbulent simulations are $20D \times 14D$ which according to figure 3.1, leads to $L_i = 4.5D$, $L_o = 14.5D$ and $H = 14D$. Beyond the boundary condition already presented in table 3.1 the boundary condition at the cylinder walls of the turbulence fields are compiled in table 4.4.

4.2.2 Initial Conditions

In RANS simulations it is necessary to have some turbulent quantities set-up at inlet, otherwise the flow predicted will be laminar since only the presence of those nonzero inlet turbulent quantities allow to switch on all relevant terms of the governing turbulent flow equations.

The initial values for the different turbulent fields depend on the initial turbulence intensity (eq. 4.3) assumed for the flow. The solutions achieved through the different turbulence models must be independent of the inlet turbulent intensity adopted. After testing inlet turbulence intensities

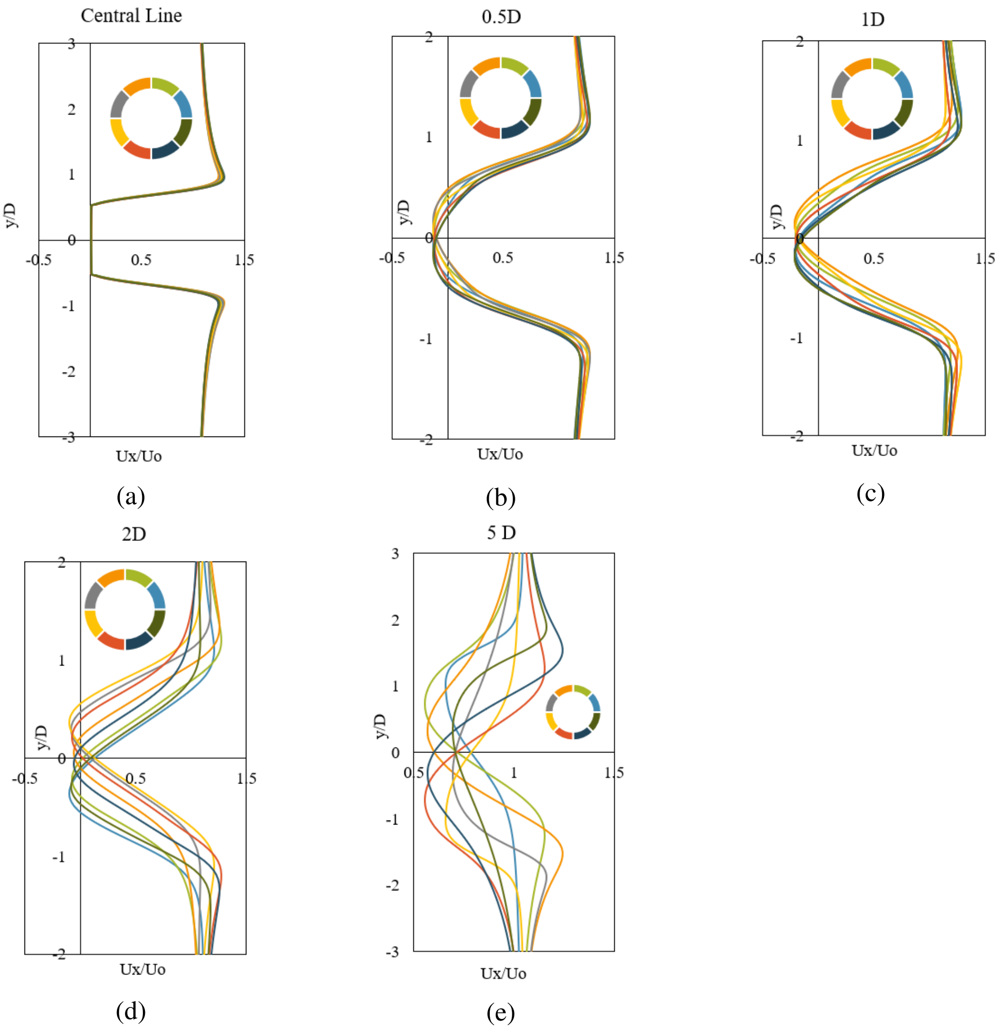

(a) (b) (c)

(d) (e)

Figure 4.7: Phase average of the velocity profiles for Re=100

Table 4.4: Boundary conditions imposed at the cylinder walls for the different turbulence fields

Field	Boundary Condition
k	kqRWallFunction
ε	epsilonWallFunction
ω	omegaWallFunction
ν_t	nutkWallFunction
γ	zeroGradient
Re_θ	zeroGradient
v^2	0
f	0

of 2%, 5% and 10% and concluding that the solutions attained were independent of the adopted value, the inlet intensity of 2% was selected.

The initial values for the turbulence properties k, ε and ω are defined by equations (4.4).

$$I = \frac{u'}{U} \tag{4.3}$$

$$k = \frac{3}{2}(UI)^2, \qquad \varepsilon = C_\mu^{\frac{3}{4}} \frac{k^{\frac{3}{2}}}{l}, \qquad \omega = \frac{\sqrt{k}}{l}, \qquad l = 0.07L \tag{4.4}$$

For the $k-\omega$ SSTLM model the intermittency (γ) and Re_θ need to initialized. This is done according to equations (4.5) and (4.6), respectively. For the v^2-f model, equation (4.7) defines the properties v^2 and f.

$$\gamma = 1 \tag{4.5}$$

$$Re_\theta = \begin{cases} 1173.51 - 589.428Tu + \frac{0.2196}{Tu^2} & \text{if } Tu <= 1.3 \\ \frac{331.5}{(Tu-0.5658)^{0.671}} & \text{if } Tu > 1.3 \end{cases}, \quad Tu = 100\frac{\sqrt{2/3k}}{|u_\infty|} \tag{4.6}$$

$$v^2 = \frac{2}{3}k_{inlet}, \qquad f = 0 \tag{4.7}$$

The discretization schemes used for most turbulence models were the backward time scheme for the time component and linearUpwind for the interpolation scheme. Because of stability problems, the interpolation scheme used for Lien-Leschziner and Lam Bremhorst $k-\varepsilon$ models was the upwind scheme, since we could not obtain converged solutions using more accurate second order schemes.

Table 4.5 compiles the results obtained for the drag coefficient, separation length and Strouhal number from the linear eddy viscosity models, the second order Reynolds stress models and the low Reynolds number turbulence models. The same table presents the relative error ε that each property has against the value used as reference. The reference used for the drag coefficient was the experimental result. The table points out the good agreement between the Reynolds stress models and the literature data. Every linear eddy viscosity model besides $k-\varepsilon$ overpredicts the drag coefficient and the Strouhal number. For the low Reynolds number turbulence models the only one with a good C_d prediction is v^2-f model.

In this flow topology, the upstream sharp cylinder corners induce flow separation that enables characteristic turbulent structures to develop. Furthermore, the turbulent wakes are not expected to be as regular as the laminar structures. In fact, looking at the streamlines and velocity contours obtained by the $k-\omega$ SST model (fig. 4.8), some characteristic features are confirmed. Besides the flow separation at the rear and at the top edge, the irregular velocity contours are characteristic of a turbulent flow around bluff bodies.

The streamline saddle points are frequently associated with high turbulence production and consequently with high Reynolds shear stresses. Although this statement cannot be adopted as

Table 4.5: Results for drag coefficient, separation length and Strouhal number for the various simulations

	C_d	$\varepsilon_{C_D}(\%)$	l/D	$\varepsilon_{l/D}(\%)$	St	$\varepsilon_{St}(\%)$
Experimental Lyn et al. (1995)	2.1	–	–	–	0.132	–
DNS Trias et al. (2015)	2.18	–	1.04	–	0.132	–
LES Sohanker et al. (2000)	2.09	–	–	–	0.132	–
LES Minguez et al. (2011)	2.2	–	1.28	–	0.141	–
$k-\varepsilon$	1.77	15.7	2.10	101.9	0.129	2.3
$k-\omega$	2.55	21.4	1.53	47.1	–	–
$k-\omega$ SST	2.47	17.6	0.76	26.9	0.145	9.8
$k-\omega$ SSTLM	2.46	17.1	0.67	35.6	0.142	7.6
Realizable $k-\varepsilon$	2.41	14.8	0.76	26.9	0.161	22.0
LRR	2.02	3.8	1.20	15.4	0.135	2.3
SSG	2.00	4.8	1.30	25	0.144	9.1
Launder Sharma $k-\varepsilon$	1.73	17.6	2.42	132.7	0.136	3.0
Lien Cubic $k-\varepsilon$	1.78	15.2	1.27	22.1	0.117	11.4
Lam Bremhorst $k-\varepsilon$	1.64	21.9	2.32	123.1	0.140	6.1
Lien Leschziner	1.65	21.4	2.25	116.3	0.140	6.1
v2f	2.01	4.3	1.38	32.7	0.145	9.8

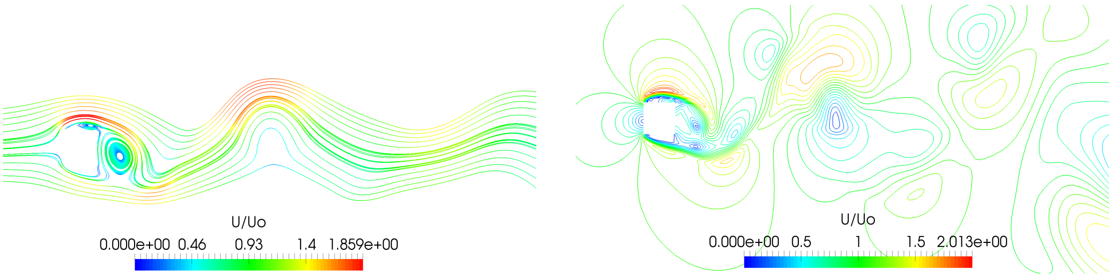

(a) (b)

Figure 4.8: Streamlines (4.8a) and contours of the streamwise velocity component (4.8b) for model $k-\omega$ SST. The colour code provides the magnitude of the normalised velocity.

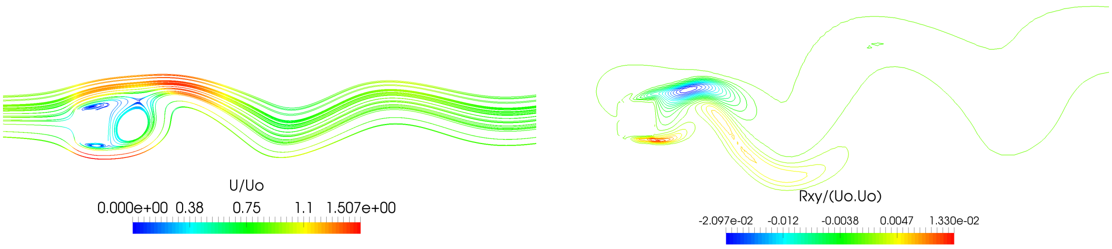

(a) (b)

Figure 4.9: Streamlines (4.9a) and contours of the Reynolds shear stress (4.9b) for LRR turbulence model. The colour code provides the magnitude of the normalised velocity and shear stress.

a rule because of the very complex flow patterns that involve turbulence (Lyn et al., 1995), it is interesting to see if such phenomenon is predicted by our simulations. Despite the Reynolds shear

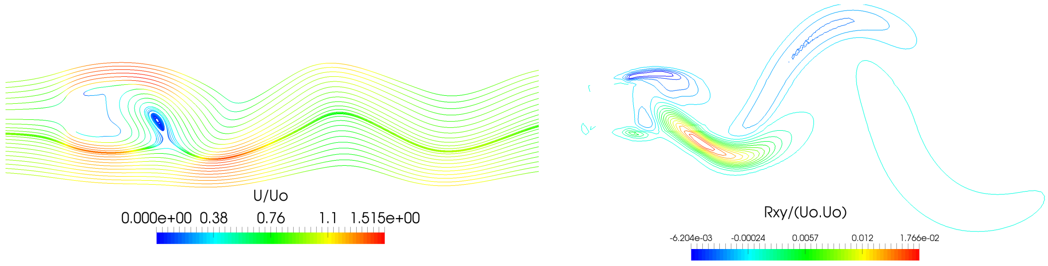

(a) (b)

Figure 4.10: Streamlines (4.10a) and contours of the Reynolds shear stress (4.10b) for the SSG turbulence model. The colour code provides the magnitude of the normalised velocity and shear stress.

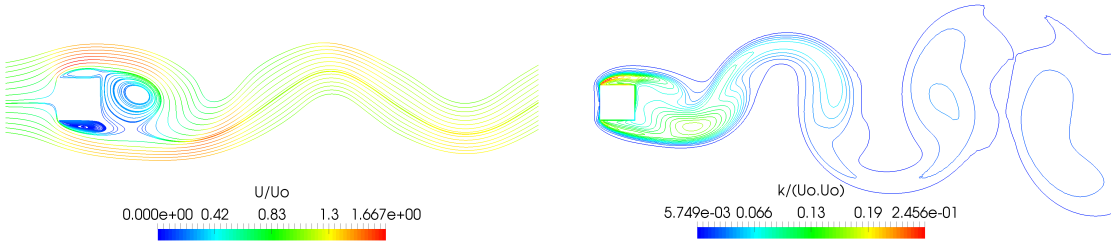

(a) (b)

Figure 4.11: Streamlines (4.11a) and contours of the turbulent kinetic energy (4.11b) for the v^2-f turbulence model. The colour code provides the magnitude of the normalised velocity and turbulent kinetic energy

stress peak attained for the LRR model (fig. 4.9b) appears to coincide with a saddle point on the flow streamlines, there is another saddle downstream without any correspondence with a shear peak. For the SSG solution (fig. 4.11) however, the saddle seen in figure 4.10a coincides with the peak in Reynolds shear stress.

Figure 4.11 shows the streamline profile of the v^2-f low Reynolds number model. The streamline representation shows a strong recirculation at the rear of the cylinder, and in the top and bottom edges. The turbulent kinetic energy plot shows the expected pulsating contours downstream of the cylinder.

Figure 4.12 together with figure 4.11b depicts the instantaneous turbulence kinetic energy k around the square block for some of the turbulence models tested. The kinetic energy production is vigorous in the shear layers bordering the wake of the cylinder, where high velocity gradients take place. The $k-\varepsilon$ turbulence model predicts excessive turbulence kinetic energy in the vicinity of the stagnant region upstream of the block. All the other models do not have this problem. It seems that the $k-\omega$ SST turbulence model generates stronger vortex shedding indicated by the more curved contours, while the $k-\varepsilon$ shows slightly long stretched vortices. Both Reynolds stress models present an intermediate situation between the $k-\varepsilon$ and $k-\omega$ SST.

Figures 4.13, 4.14 and 4.15 presents the normalized time averaged turbulent kinetic energy

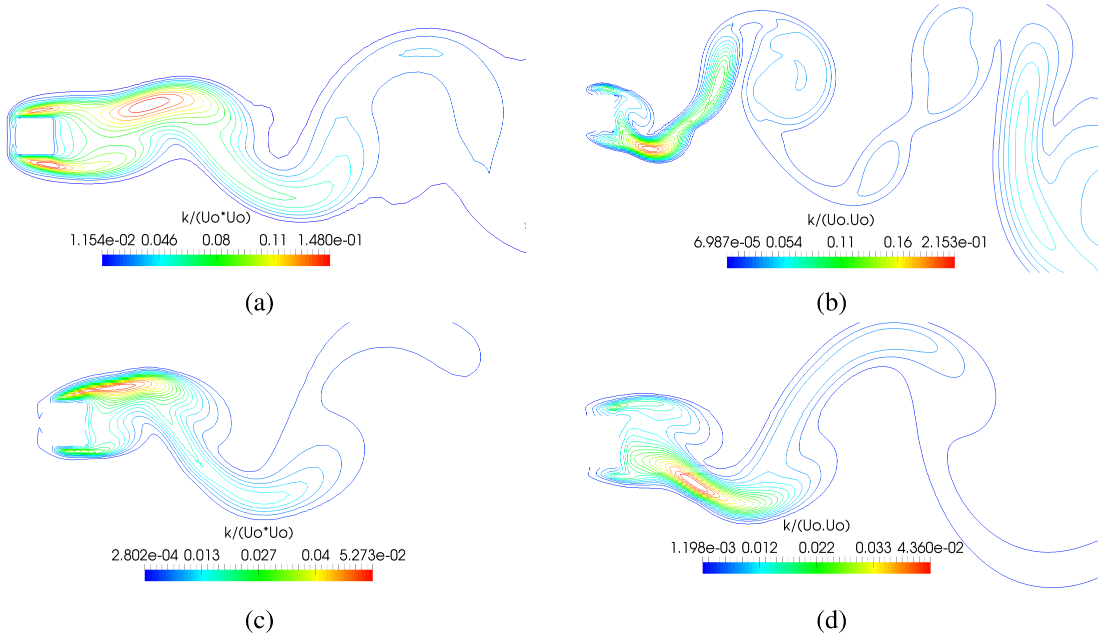

(a) (b)

(c) (d)

Figure 4.12: Contour plots of the normalized turbulent kinetic energy for some turbulence models: $k-\varepsilon$ (a), $k-\omega$ SST (b), LRR (c) and SSG (d)

for the eddy viscosity models, the Reynolds stress models and the low Reynolds number turbulence models, respectively. These plots also present the experimental results obtained by Lyn in 1990, taken from Franke and Rodi (1991). As we can see from these plots, all turbulence models underestimate the kinetic energy along the symmetry plane downstream of the flow. Despite the intensity differences, it is clear that some of the plots present the same shape as the experimental result. Looking particularly at the $k-\omega$ SST, $k-\omega$ SSTLM, realizable $k-\varepsilon$, both Reynolds stress models and $\overline{v^2}-f$ model, we see similitudes in the plot shapes, in spite the peak of k being shifted to the left, in every case. In figure 4.14 we present the $k-\omega$ SST and $k-\omega$ SSTLM together with the Reynolds stress model results to show the different order of magnitude in the kinetic energy predictions by these two sets of models. From these figure, it is clear that the $k-\omega$ SST, $k-\omega$ SSTLM and $\overline{v^2}-f$ are closer to the experimental results. Figure 4.15 shows how different the results from the various low Reynolds number turbulence models are from each other. That said, taking into account the shape of the graphs we can say that the Launder-Sharma $k-\varepsilon$ and $\overline{v^2}-f$ models provide the closest results to the experimental points.

Figure 4.16 represents the downstream evolution of the turbulent kinetic energy profiles for some of the turbulence models tested. These plots are in agreement with the previous figures: the LRR model predicts the less amount of turbulent kinetic energy and $\overline{v^2}-f$ the most

A brief view on the mesh parameters used for the different simulations are shown in table 4.6. Further details on the grid characteristics are presented in appendix B. It is important to point out that the $k-\omega$ SST and SSG turbulence models results were calculated using a distinct mesh than the other turbulence models despite having all the same number of cells along the cylinder side. The difference in cell number upstream and downstream of the cylinder was balanced with

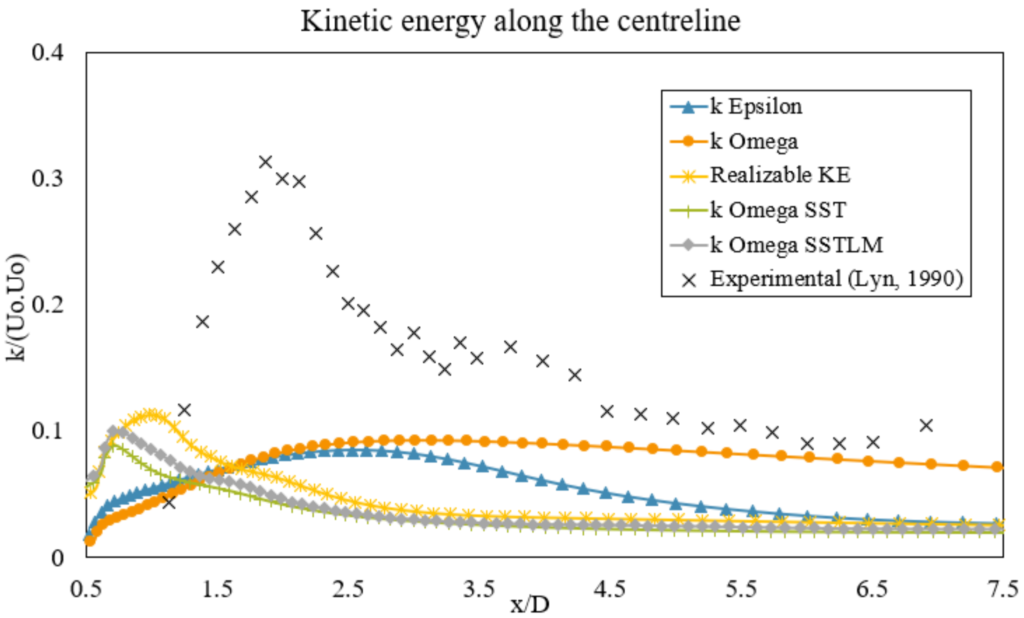

Figure 4.13: Linear eddy viscosity results for the normalised profiles along the flow symmetry line

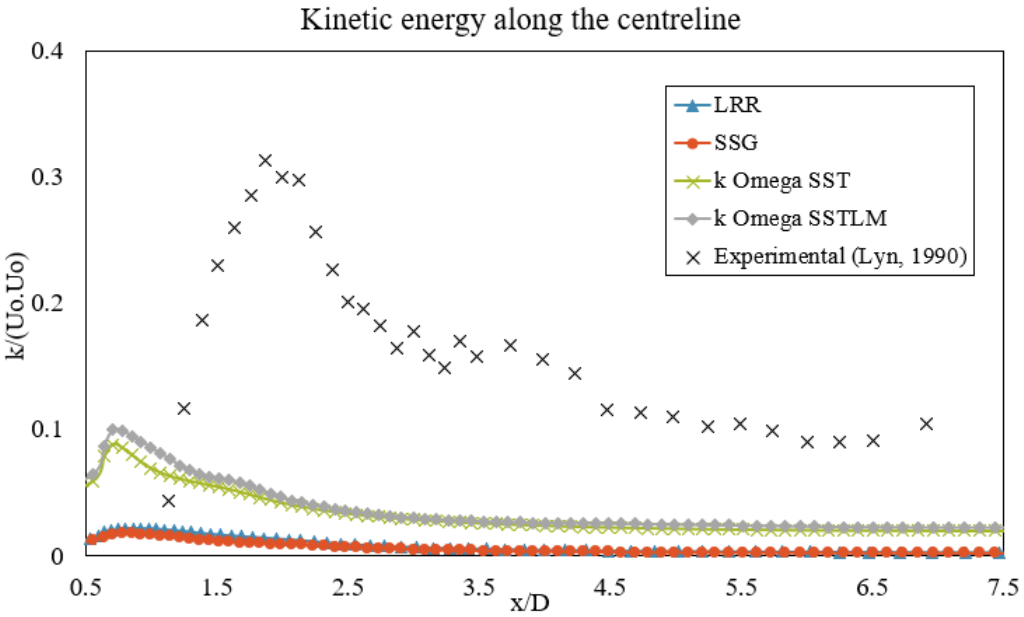

Figure 4.14: Reynolds stress results for the normalised profiles along the flow centre line

appropriate expansion factors in such a way that a similar y^+ along the first grid line of our domain was attained.

Figures 4.17, 4.18a and 4.18b present the evolution of the drag coefficient with time for the simulations executed. Figures 4.20, 4.20a and 4.20b show the evolution of the separation length at the cylinder rear with time for the simulations executed. The $k-\omega$ model does not predict any oscillation on both the drag coefficient and the separation length. The remaining models, as expected predict oscillatory behaviour that is superimposed on the turbulent fields. Furthermore,

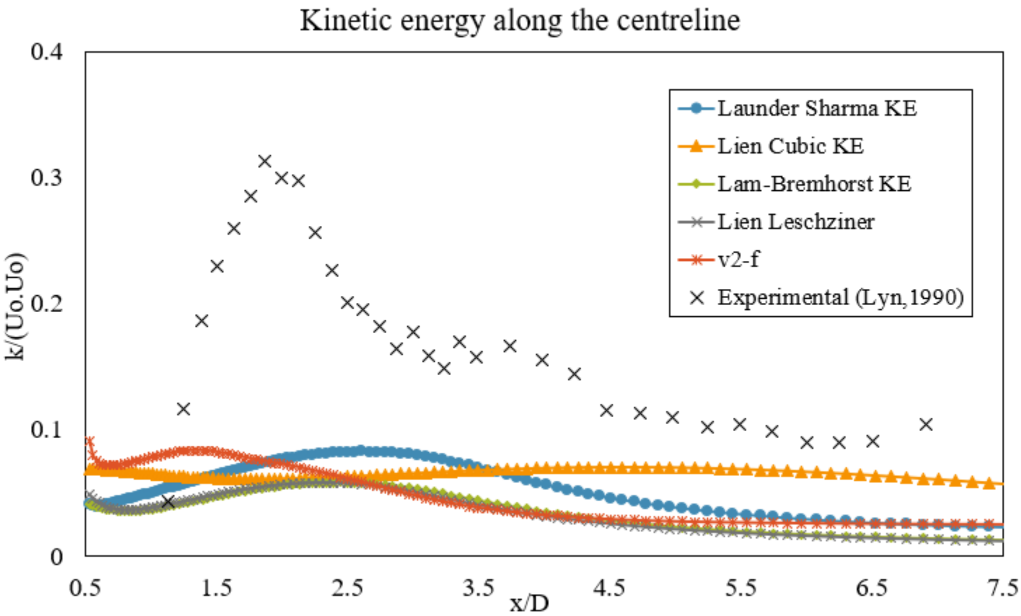

Figure 4.15: Low Reynolds number results for the normalised profiles along the flow centre line

Table 4.6: Grid refinement used for the linear eddy viscosity models simulations

Turbulence model	Number of cells	Cells around cylinder face
$k-\varepsilon$	13345	21
$k-\omega$	13345	21
$k-\omega$ SST	27587	21
$k-\omega$ SSTLM	13345	21
Realizable $k-\varepsilon$	13345	21
LRR	13345	21
SSG	27587	21
Low Reynolds number	45536	43

we can see that while some models present a regular shedding oscillation, the $k-\omega$ SST and $k-\omega$ SSTLM and Lien Cubic $k-\varepsilon$ turbulence models show what seems to be a superimposition of different shedding frequencies.

The lift coefficient power spectra for the different models are presented in figure 4.21 and confirm these observations: whereas the $k-\varepsilon$ (fig. 4.21a) and the Realizable $k-\varepsilon$ (fig. 4.21d) present a very distinctive, unique frequency for the vortex shedding, the $k-\omega$ SST (fig. 4.21b) and the $k-\omega$ SSTLM (fig. 4.21d) show multiple frequencies with significant intensity on the shedding process. The same analysis can be carried out for the other turbulence models: besides the Lien Cubic $k-\varepsilon$ spectrum (fig. 4.21h), which presents a superposition of different frequencies, the remaining low Reynolds number models (fig. 4.21) and both Reynolds stress turbulence models show spectra with a single peak representing a single shedding frequency. From literature we see that a single characteristic shedding frequency does not occur in experimental flows of this kind. These results are a consequence of the oversimplifications the models give to the turbulence

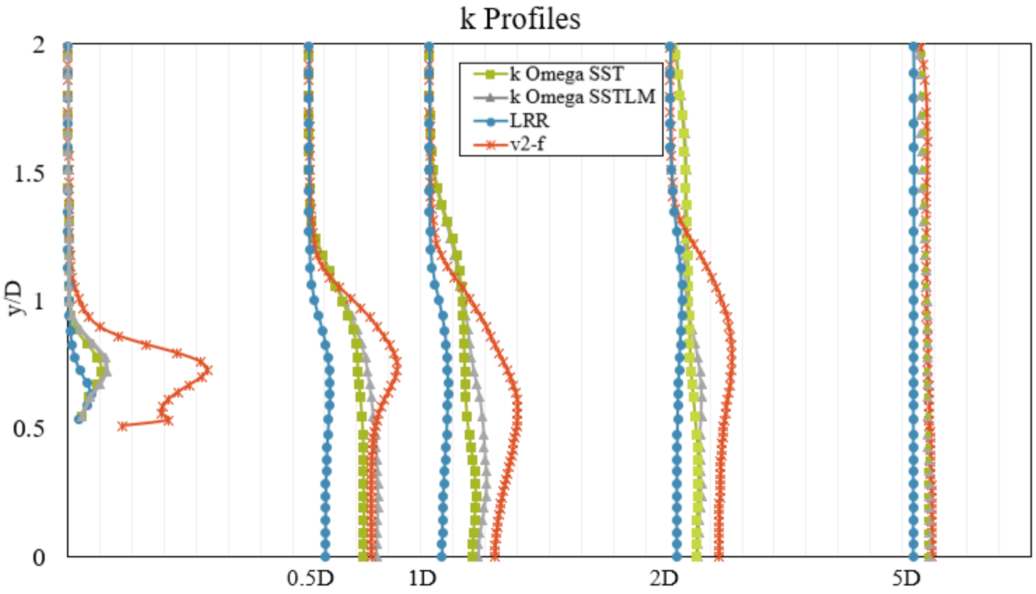

Figure 4.16: Turbulent kinetic energy profiles downstream of the flow for some turbulence models

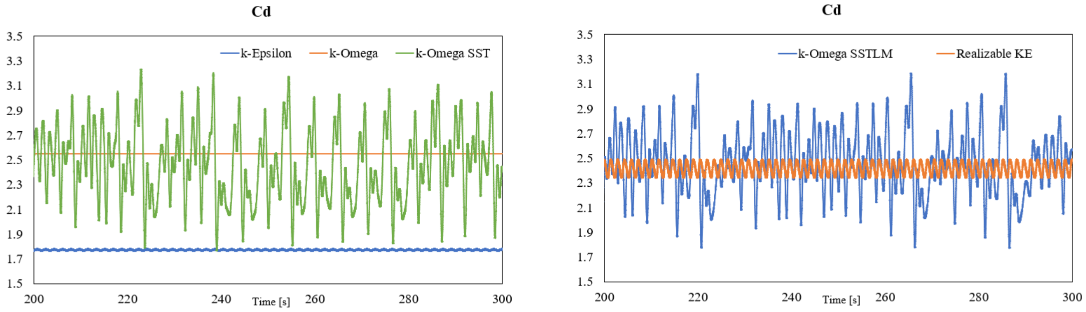

(a) (b)

Figure 4.17: Drag coefficient evolution for $k-\varepsilon$, $k-\omega$, $k-\omega$ SST, $k-\omega$ SSTLM and realizable $k-\varepsilon$ models

phenomenon.

A comparison of the time averaged velocity profiles for the different linear eddy viscosity turbulence models and the experimental data is presented in figure 4.22. Overall, the $k-\omega$ SST and $k-\omega$ SSTLM exhibit a good alignment with the experimental data in the base flow region. The poor performance of the $k-\omega$ model in the near-wall region (especially at the cylinder centre line) is in contradiction with the literature that predicts a good performance of this model on that zone. Furthermore, the presupposed better behaviour of the $k-\omega$ compared to the $k-\varepsilon$ model is not seen at the cylinder centre line, although it betters at $x = 0.5D$. As expected, the $k-\varepsilon$ model performs poorly in the region closer to the centre line and better in free shear region of the flow. The realizable $k-\varepsilon$ result presents a clear improvement from the standard $k-\varepsilon$ model, despite the incorrect prediction in the downstream flow region.

Figure 4.23 presents a comparison of the velocity profiles at the cylinder axis $y = 0$. Thought

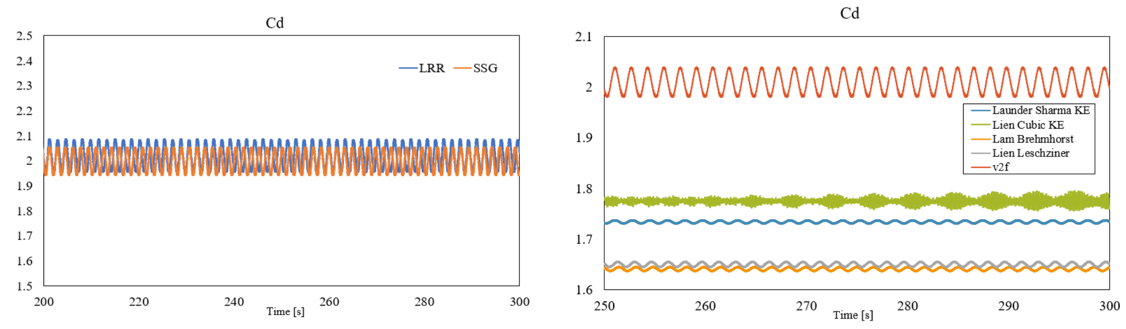

(a)

(b)

Figure 4.18: Drag Coefficient evolution for the Reynolds Stress turbulence models (4.18a) and the low Reynolds number turbulence models (4.18b)

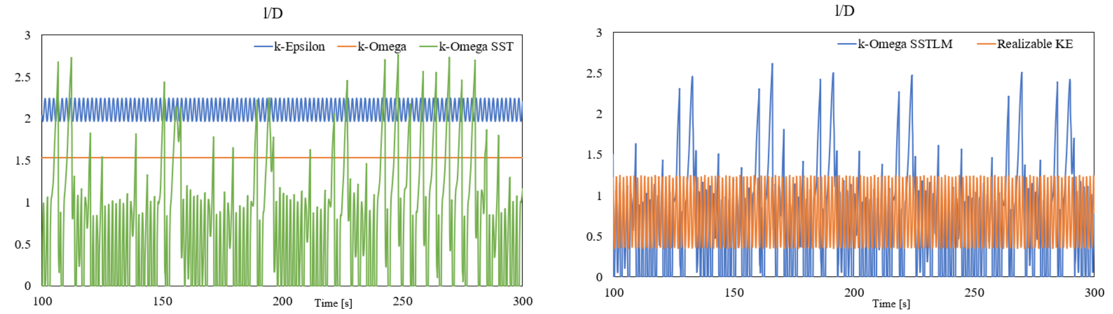

(a)

(b)

Figure 4.19: Evolution of the separation length for $k-\varepsilon$, $k-\omega$ and $k-\omega$ SST, $k-\omega$ SSTLM and realizable $k-\varepsilon$ models

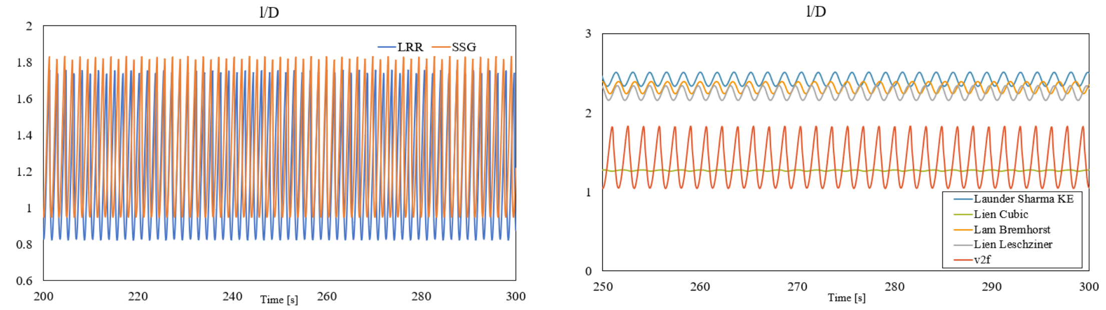

(a)

(b)

Figure 4.20: Evolution of the separation length for the Reynolds stress models (4.20a) and the low Reynolds number models (4.20b)

the realizable $k-\varepsilon$, $k-\omega$ SST and $k-\omega$ SSTLM predict a good recirculation zone (compared to the experimental points), they lack accuracy downstream of the flow by over-predicting the velocity recovery. The $k-\varepsilon$ and $k-\omega$ have the worst performance not only because of the separation length but also for the underpredicted velocity recovery downstream of the flow.

The same comparisons for the time-averaged profiles attained the Reynolds stress turbulence models (figure 4.24) shows a good approximation between both models and the experimental data

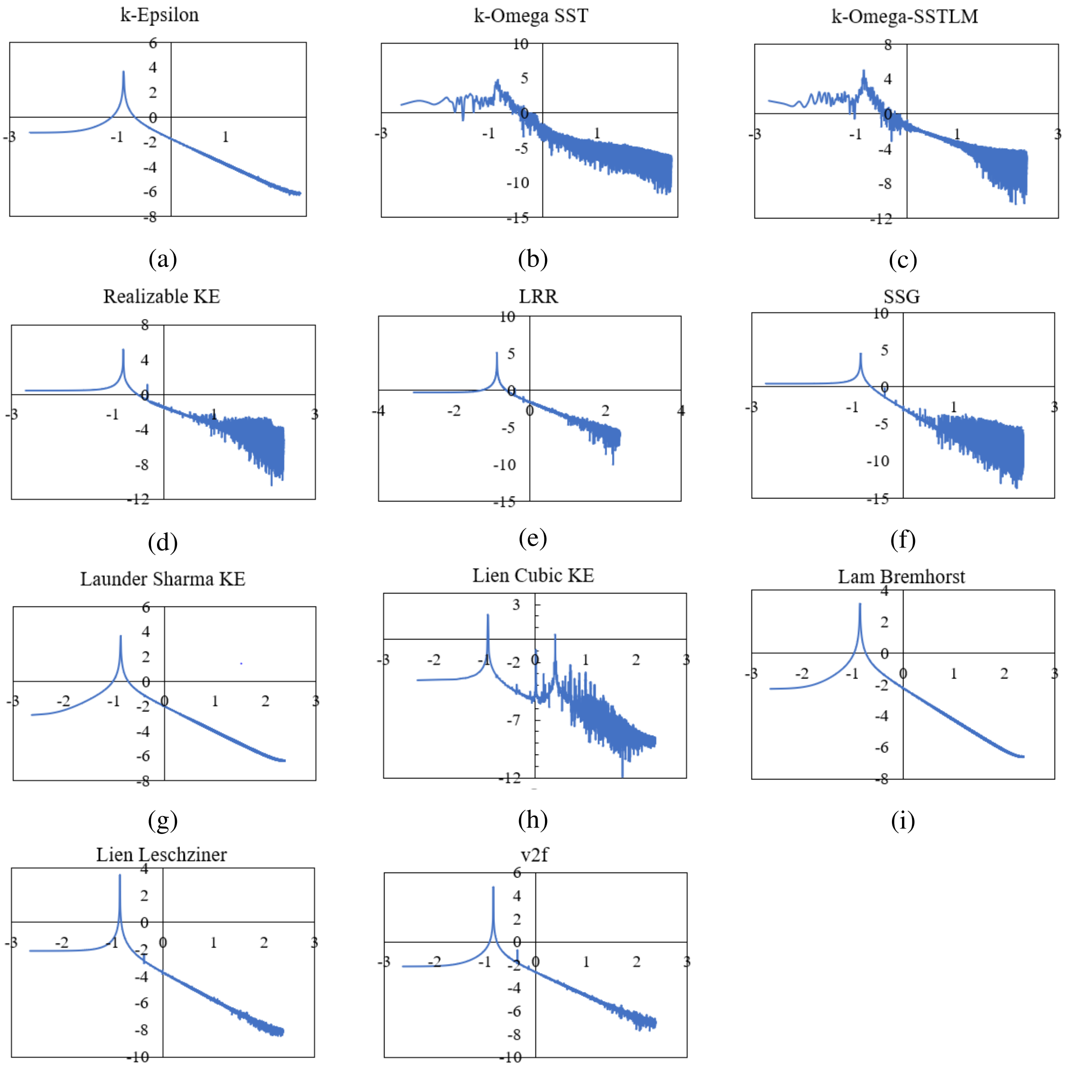

(a) (b) (c) (d) (e) (f) (g) (h) (i) (j) (k)

Figure 4.21: Power spectrum of the lift coefficient for the linear eddy viscosity turbulence models (figs. 4.21a - 4.21d) and for the Reynolds stress turbulence models (figs. 4.21e and 4.21f) and low Reynolds number turbulence models (figs. 4.21g - 4.21k)

particularly in the wake region closer to the cylinder (0.5D). For comparison purpose, we present once again the $k-\omega$ SST and $k-\omega$ SSTLM models since they presented the best reults from the eddy viscosity models. We should notice that both sets of models offer similar results in most flow regions. That said, in the regions closer to the cylinder axis, the eddy viscosity profiles appear closer to the experimental points.

The separation length and the velocity recovery along the centre line downstream of the flow are over-predicted by the Reynolds stress models (figure 4.25). Once again the eddy viscosity results are in with better agreement with the experimental data.

Although both Reynolds stress models tested show very similar results, the velocity profiles reveal the LRR model with better alignment with the experimental points.

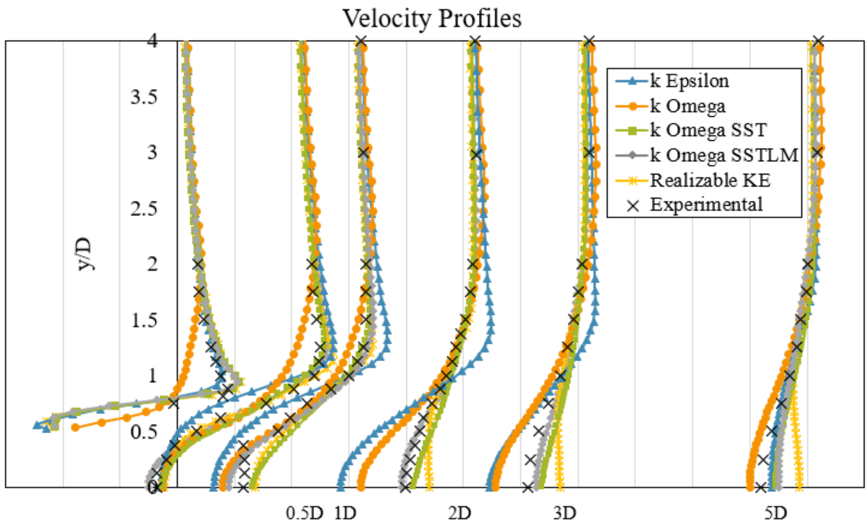

Figure 4.22: Comparison between transverse profiles of the time-averaged streamwise velocity at different stations downstream the cylinder for the linear eddy viscosity models

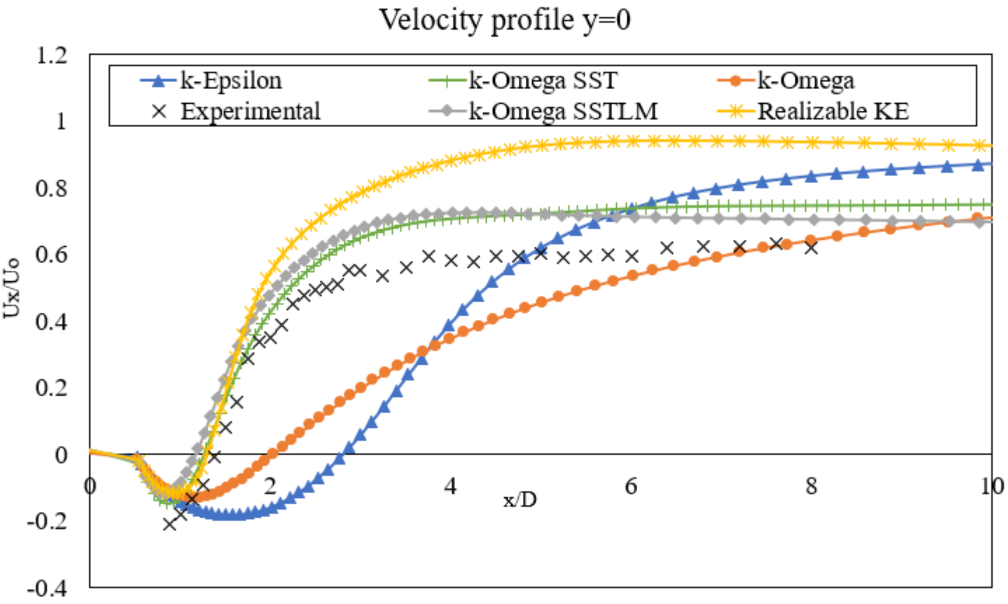

Figure 4.23: Comparison of the streamwise normalized velocity along the symmetry centreplane predicted by the turbulence models

In annex D is shown a comparison between the Reynolds stresses attained from these models with experimental data. As we can see, there is an overall under prediction of these properties in these models.

From the overall analysis we conclude that, despite the good numerical results obtained from the Reynolds Stress Models (table 4.5), we see that the velocity profiles predicted from the two eddy viscosity models are overall more accurate. This way, we consider that these two eddy viscosity models predict a better flow prediction than the Reynolds stress turbulence models.

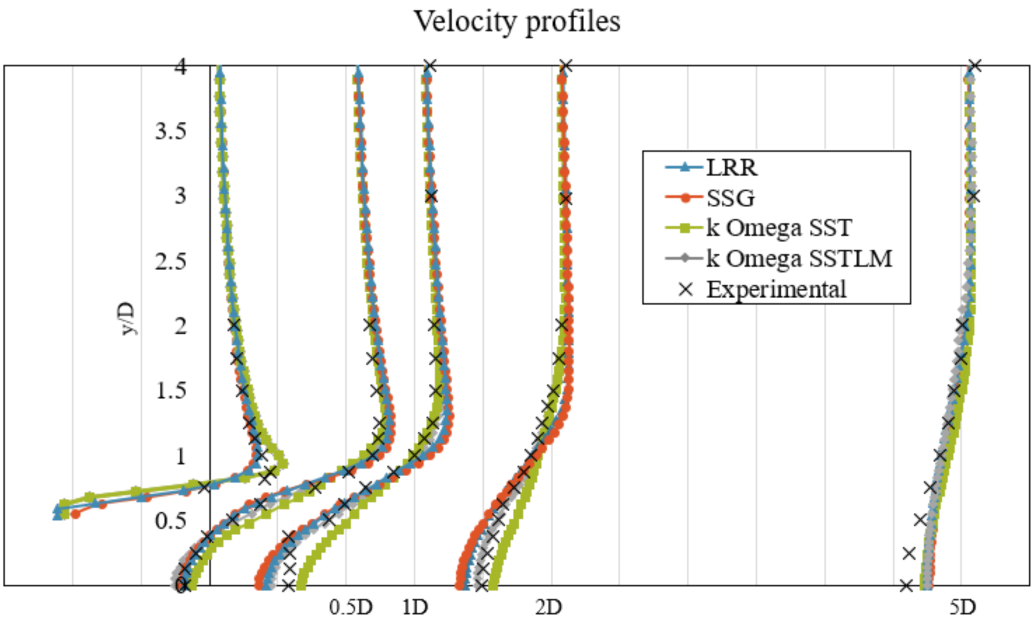

Figure 4.24: Evolution of the velocity profiles for the Reynolds stress models and the $k-\omega$ SST and $k-\omega$ SSTLM eddy viscosity models

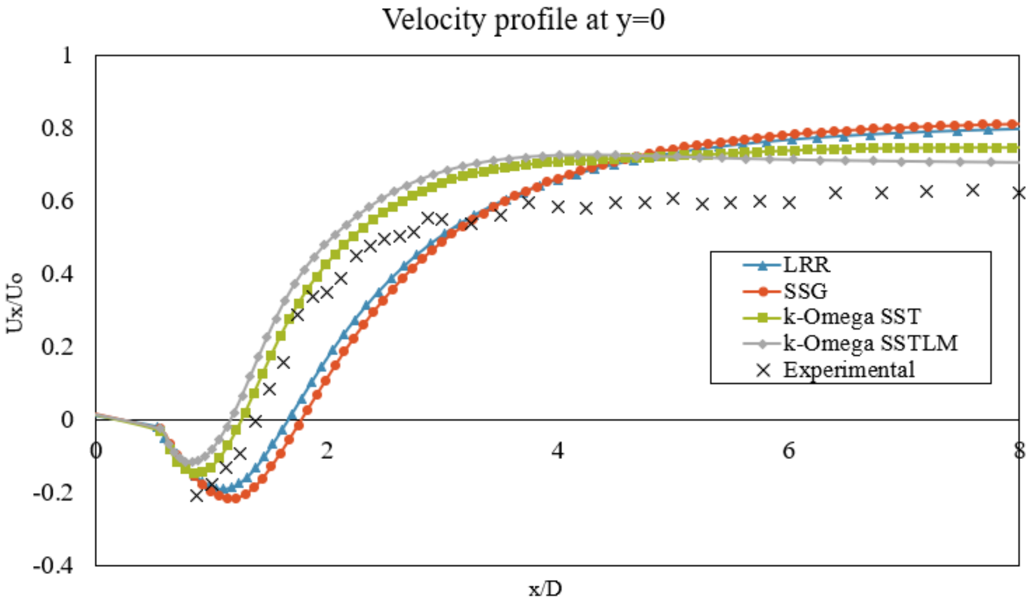

Figure 4.25: Streamwise velocity along the symmetry centreplane for the Reynolds stress models and $k-\omega$ models

For the low Reynolds turbulence models profiles (fig. 4.26) we see that at 2D the $\overline{v^2}-f$ model is in good agreement with the experimental points. However that agreement seems to be momentary since it is not replicated 5D away from the cylinder.

The profiles at $y=0$ (fig. 4.27) show that most low Reynolds turbulence models show profiles that are very far from the experimental points. Despite the separation length predicted by the Lien

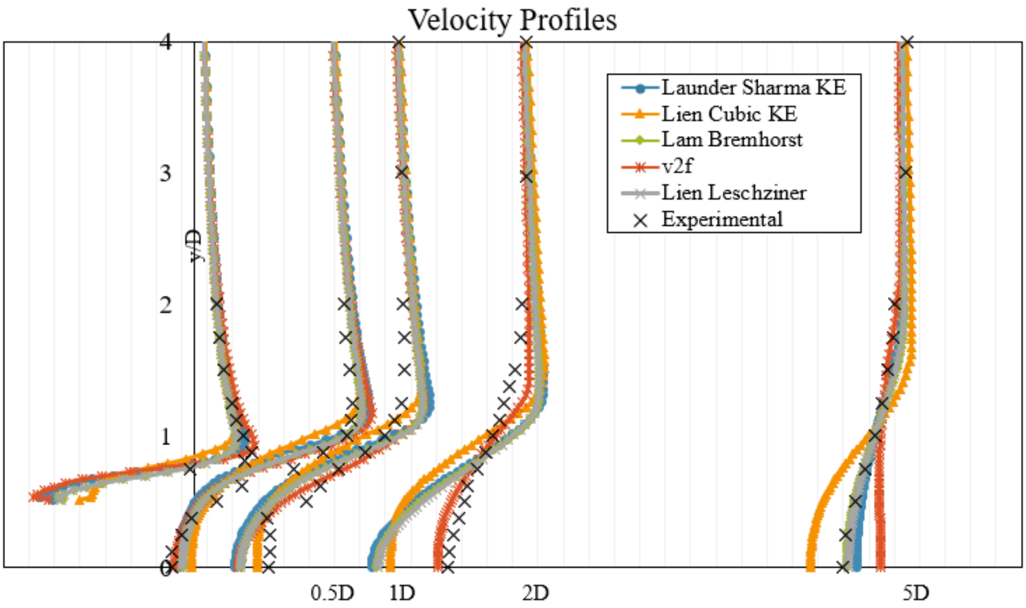

Figure 4.26: Comparison of velocity profiles between the low Reynolds number turbulence models and the experimental data

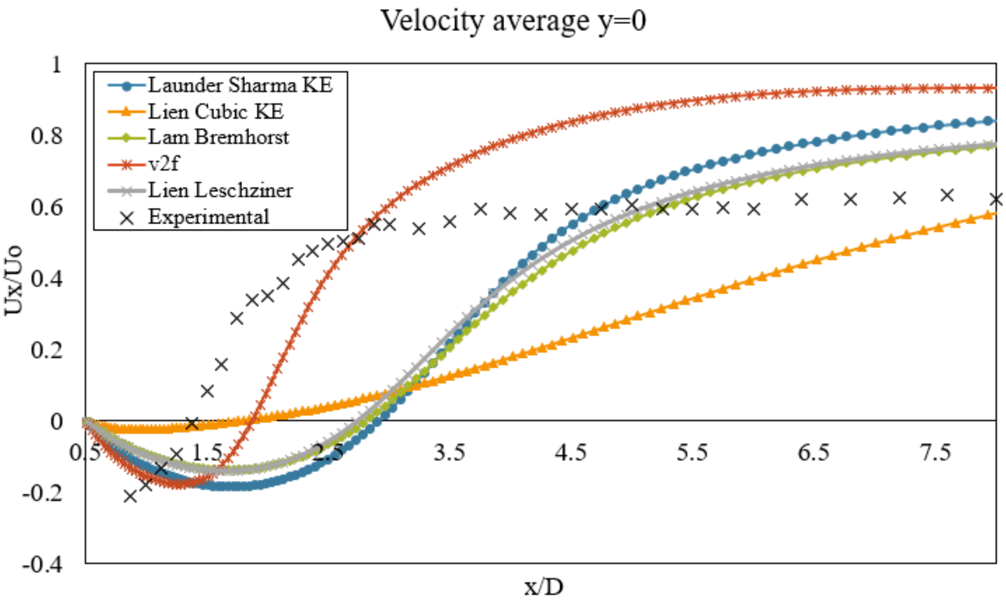

Figure 4.27: Comparison of the streamwise normalized velocity along the symmetry centreplane predicted by the turbulence models

Cubic $k-\varepsilon$ being close to the experimental result, the velocity variation along the downstream flow is very far from the experimental counterpart. Once again, the $\overline{v^2}-f$ turbulence model gives the best result.

We should not forget that, as it was mentioned in the beginning of this section, the interpolation scheme used for the simulations with Lam-Bremhorst $k-\varepsilon$ and Lien Leschziner models was the first order upwind because of stability problems with higher order schemes. This factor for sure had a major impact on the poor performance of both this models.

In annex C we present the phase-averaged velocity profiles for the various simulations proceeded.

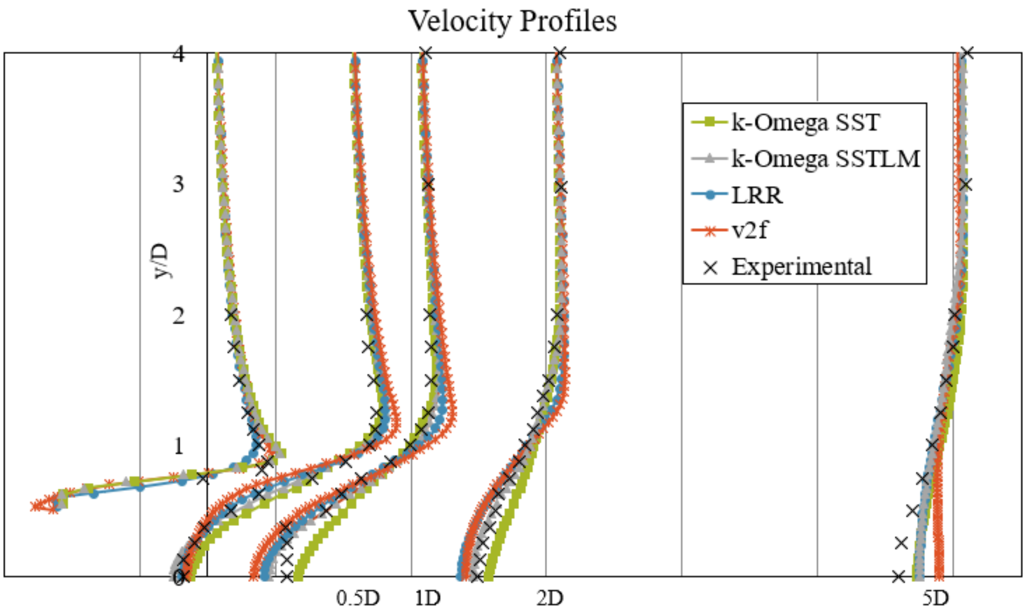

Figure 4.28: Velocity profiles comparison between the best results obtained through the simulations

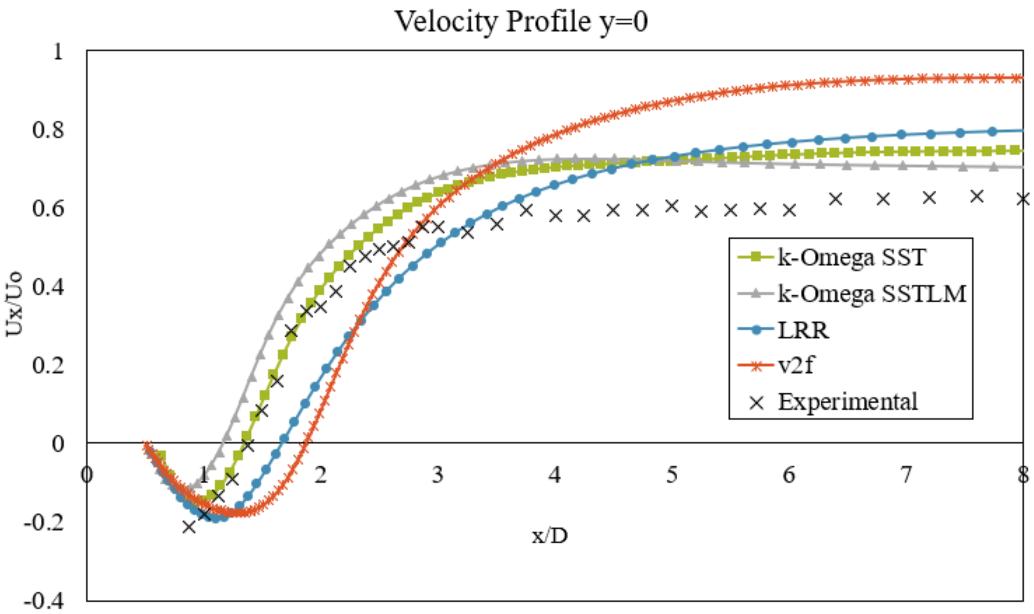

Figure 4.29: Streamwise velocity along the symmetry centreplane from the best turbulence models

From the different analysis proceeded through the project, the best results came from the $k-\omega$ SST, $k-\omega$ SSTLM, LRR and $\overline{v^2}-f$ turbulence models.

We should not forget that the $k-\omega$ SSTLM was designed to be applied in flows where the laminar-turbulent transition is present. That said, this model derives from the $k-\omega$ SST model, since it uses the two transport equations of the second one plus the transient correlations. This way, the good performance seen from this model was surprising to see but expected at the same time.

In figures figures 4.28 and 4.29 a compilation of the results from the best models is presented. From these plots, we notice that the eddy viscosity models continue to give better predictions compared to other turbulence models. However, looking at the numerical results in table 4.5 we are reminded that, despite the accurate mean flow description, these models lack accuracy in the numerical results obtained.

There are other variables to take into account when making a decision for what turbulence model to use. The linear eddy viscosity turbulence models, because of their simplicity, didn't require much time to reach a solution. On the other hand the Reynolds stress models and the low Reynolds number models took longer time to simulate. The former due to the extra transport equations for the Reynolds stresses and the latter because of the good mesh refinement it requires near wall regions.

4.3 Rectangular case

As mentioned throughout this text, one of the flow features of the turbulent flow around the square cylinder is the the attached and detached shear layers on the side walls. However, in the square the size of the obstacle in the streamwise direction is too small for the size in the transverse direction and the flow never has the occasion to reattach. By using a rectangular cylinder the capability of the models to predict also reattachment can be evaluated.

This way, some simulations using some of the turbulence models are now repeated to the flow around a rectangular cylinder.

Figure 4.30 presents the geometry used for these simulations. The wall functions and inlet values for the different properties were the same as the ones applied for the square case simulation. According to this figure, $L_i = 4.5D$, $L_o = 21.5D$ and $H = 14D$. The aspect ratio of the rectangular section was 4.

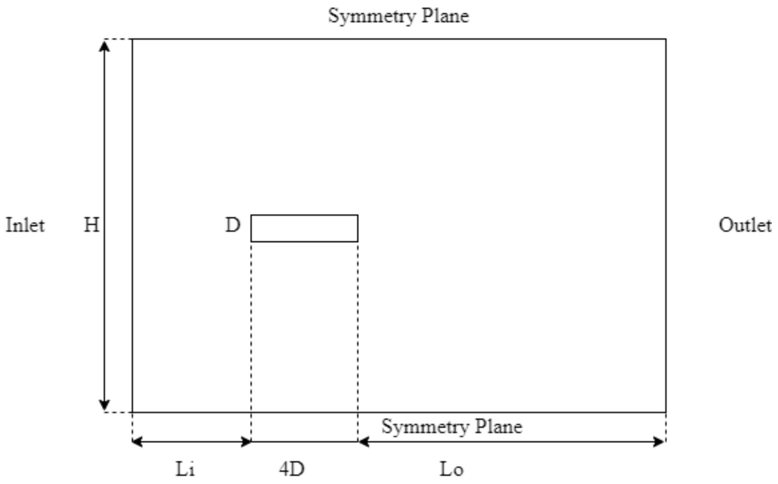

Figure 4.30: Rectangular geometry setup

The streamlines and velocity contours show very well the phenomena of detachment and reattachment that occurs in the top edge of the rectangular section. Figure 4.31e is particularly good in depicting this double separation that occurs periodically.

Notice that the $k-\omega$ SST model predicts a Kármán vortex street in the wake region (fig. 4.31b), with regions of high and low vorticity disposed symmetrical in relation to the streamwise axis. The same contours for the Reynolds stress models are not symmetrical.

Table 4.7 shows the average distance from the sharp edge of the rectangle that the flow separates and then reattaches. It also shows the average separation length for the tested turbulence models.

It is curious to notice that according to these results, the flow does not separate at the upstream corner but a little bit further downstream. Because of the oscillating nature of the flow, the separation length along the rectangle side also oscillates with time (fig. 4.32).

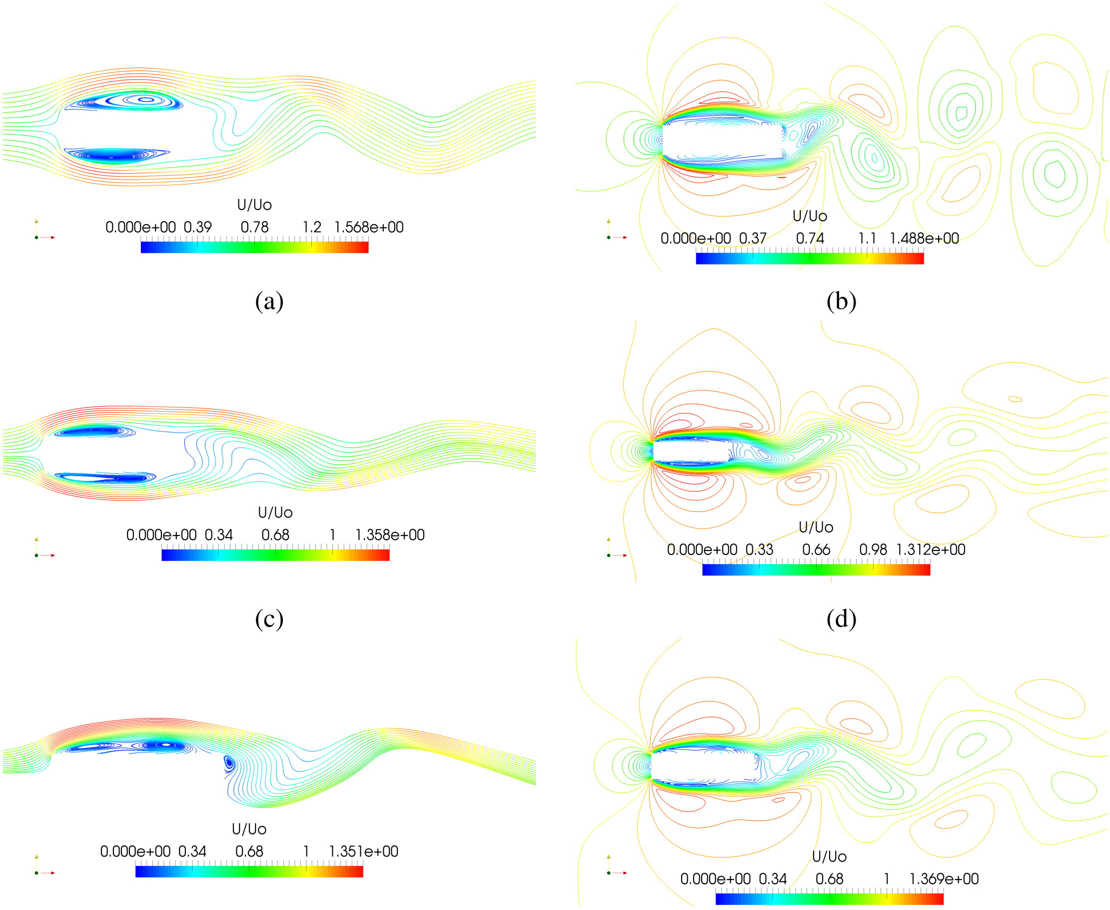

(a) (b)

(c) (d)

(e) (f)

Figure 4.31: Streamlines and velocity contours obtained from the $k-\omega$ SST (4.31a and 4.31b), LRR (figs. 4.31c and 4.31d) and SSG (4.31e and 4.31f),

Table 4.7: Separation and reattachment points along the rectangle side and average separation length

	Separation point	Reattachment point	Separation length
$k-\omega$ SST	0.11	3.41	3.30
LRR	0.26	3.23	2.97
SSG	0.27	2.95	2.68

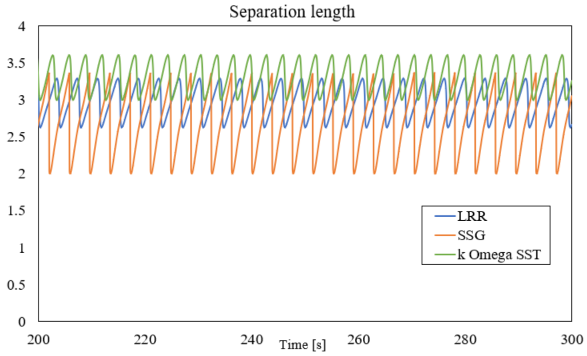

Figure 4.32: Evolution of the separation length along the rectangle side with time

Chapter 5

Conclusion

The goal of this project was to make a comparative analysis between the different existing numerical CFD models in a turbulent flow around a square cylinder. Several turbulence models were tested and their results promptly discussed.

Despite their simplicity and low cost, the linear eddy viscosity models presented good description of the flow properties. That said, it was also clear that some of the simplifications made by these models originated unrealistic results. The more clear example is the absence of flow oscillation predicted by the $k-\omega$ model.

Despite the poor numerical results attained from the $k-\omega$ SST and $k-\omega$ SSTLM turbulence models, these algorithms offer a very good relation between the quality of the results and the computational cost they require. These models presented a relatively good description of the shedding process in the wake region showing structures like the separation bubble and the vortex street along the wake, as well as a good representation of the turbulent kinetic energy along the flow symmetry line.

In the rectangular case, we could also see the reattachment of the flow along the cylinder edge and measure the recirculation length of this separation bubble.

The low Reynolds number turbulence models require more computational cost due to the mesh refinement and even when some result attained seems better than the eddy viscosity counterpart (for example the $\overline{v^2}-f$ numerical results) they do not compensate the inflated cost.

A next step for this work is to perform a LES simulation to attain a more accurate flow description, despite the increased computational cost. In this case, we would expect a better agreement with the published data, both in the numerical results and the main flow features like the vortex shedding on the cylinder wake and the velocity profiles.

Appendix A

User interface in *OpenFOAM*

OpenFOAM is an open source CFD code developed in *C++* language. It has pre-processing and post-processing utilities for the solution of continuum mechanics problems. This software is most commonly used in *LINUX* operating system.

The base case for most *OpenFOAM* applications contains three folders: the *system* folder, the *0* folder and the *constant* folder (fig. A.1).

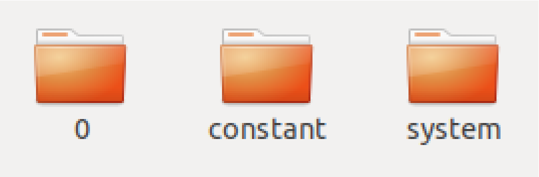

Figure A.1: *OpenFOAM* base case

The *0* folder contains dictionaries with the initial state of the various properties to be solved through the simulation (fig. A.2). Generally this folder contains dictionaries for the initial pressure p, velocity U and some turbulence properties like the turbulent kinetic energy k (for a turbulent simulation). Each property is then calculated in each time step of the simulation.

Figure A.2: *0* folder

The *constant* folder contains the dictionaries *transportProperties* and *turbulenceProperties* (fig. A.3). In the first one the user specifies the fluid properties (e.g. kinematic viscosity). The second dict is only present in a turbulent simulation and it specifies the simulation type (e.g. RAS or LES) and the turbulence model to be applied (e.g. $k-\varepsilon$ model). Furthermore the *constant* folder also contains a *polymesh* folder which has the different files necessary to build the geometry of our mesh.

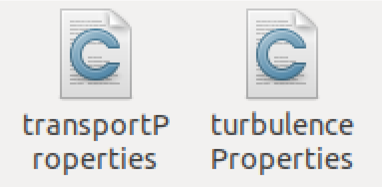

Figure A.3: *constant* folder

The *system* folder sets parameters associated with the solution procedure (fig. A.4). The *blockMeshDict* enables the user to build the geometry domain: the vertices necessary to build the different blocks and patches are specified and named. The *controlDict* sets the run control parameters including the time step of the simulation and the parameters for data output. Using the *fvSchemes* dict the user specifies the necessary discretization schemes to be applied in the various terms such as the interpolation, diffusion and time schemes. *fvSolution* dict enables the user to specify the equation solvers, desired tolerances and other algorithm control.

Figure A.4: *system* folder

Appendix B

Mesh parameters

Figure B.1 shows the 8 blocks that constitute the structure of our mesh. Each block was divided into cells in the x and y directions. The number of those divisions and the expansion factors used for the for the different simulations are compiled in tables B.1, B.2 and B.3.

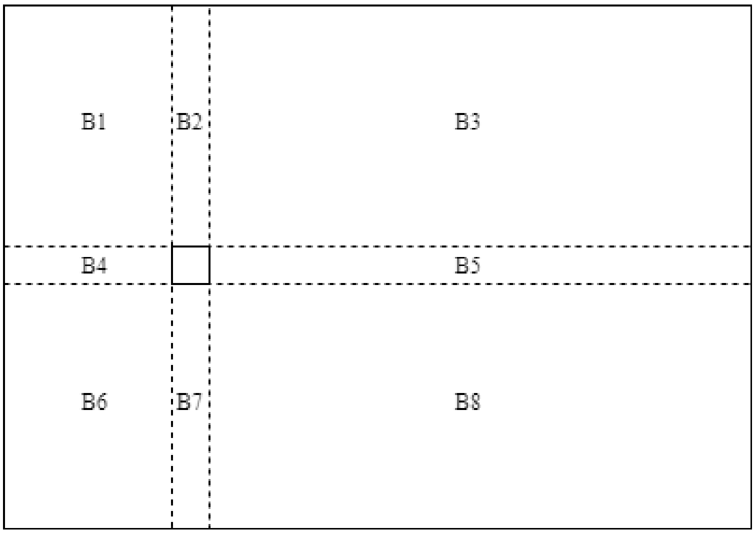

Figure B.1: Blocks that constitute our mesh

Table B.1: Mesh parameters used for the simulations with $k-\varepsilon$, $k-\omega$, $k-\omega$ SSTLM, Realizable $k-\varepsilon$ and LRR turbulence models

Block	Nº cells x direction	Expansion factor	Nº cells y direction	Expansion factor
B1	24	0.125	45	8
B2	21	1	45	8
B3	75	10	45	8
B4	24	0.125	21	1
B5	75	10	21	1
B6	24	0.125	45	0.125
B7	21	1	45	0.125
B8	75	10	45	0.125

Table B.2: Mesh parameters used for the simulations with $k-\omega$ SST and SSG turbulence models

Block	Nº cells x direction	Expansion factor	Nº cells y direction	Expansion factor
B1	48	0.5	60	4
B2	21	1	60	4
B3	125	2.5	60	4
B4	48	0.5	21	1
B5	125	2.5	21	1
B6	48	0.5	60	0.25
B7	21	1	60	0.25
B8	125	2.5	60	0.25

Table B.3: Mesh parameters used for the low Reynolds number turbulence models simulations

Block	Nº cells x direction	Expansion factor	Nº cells y direction	Expansion factor
B1	48	0.125	75	8
B2	43	1	75	8
B3	150	10	75	8
B4	48	0.125	43	1
B5	150	10	43	1
B6	48	0.125	75	0.125
B7	43	1	75	0.125
B8	150	10	75	0.125

Appendix C

Phase Averaged Velocity Profiles

C.1 Linear Eddy Viscosity Models

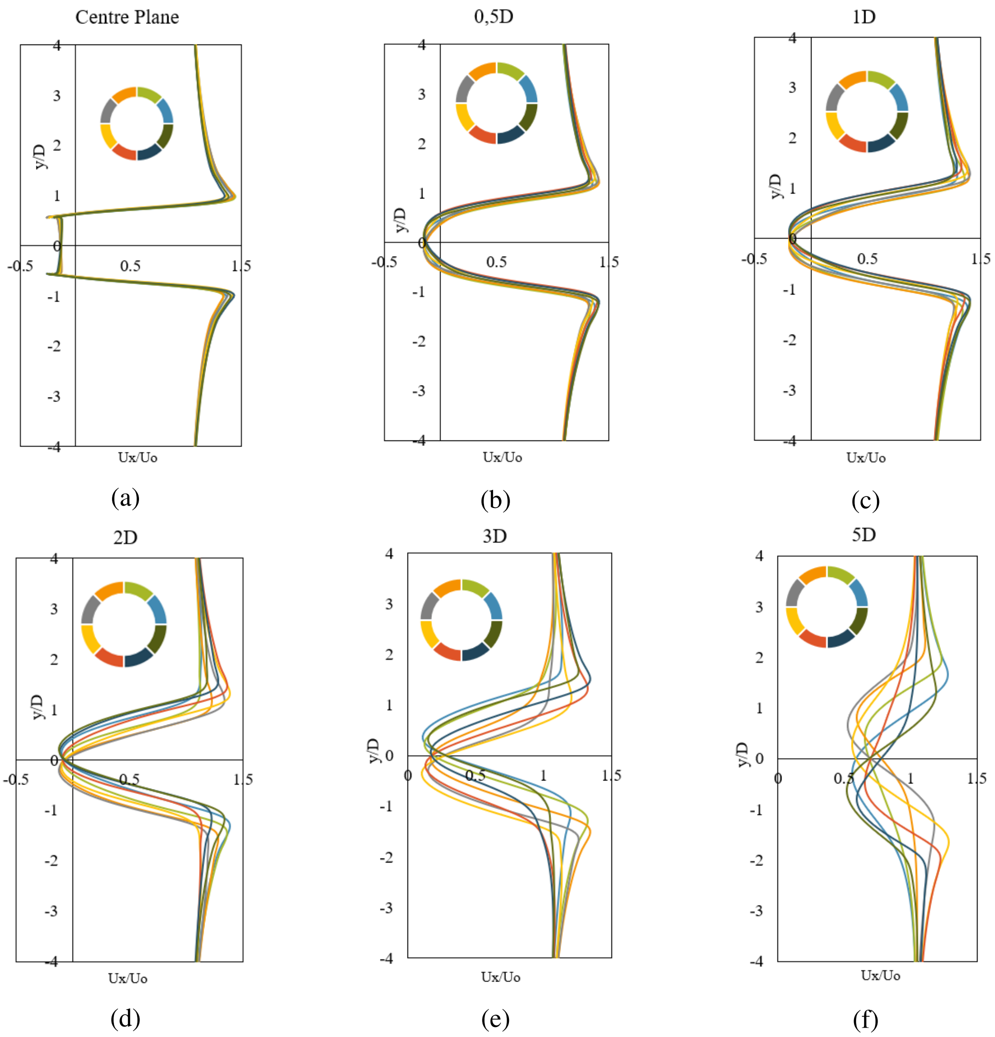

(a) (b) (c)

(d) (e) (f)

Figure C.1: Phase-averaged velocity profiles for the $k-\varepsilon$ model

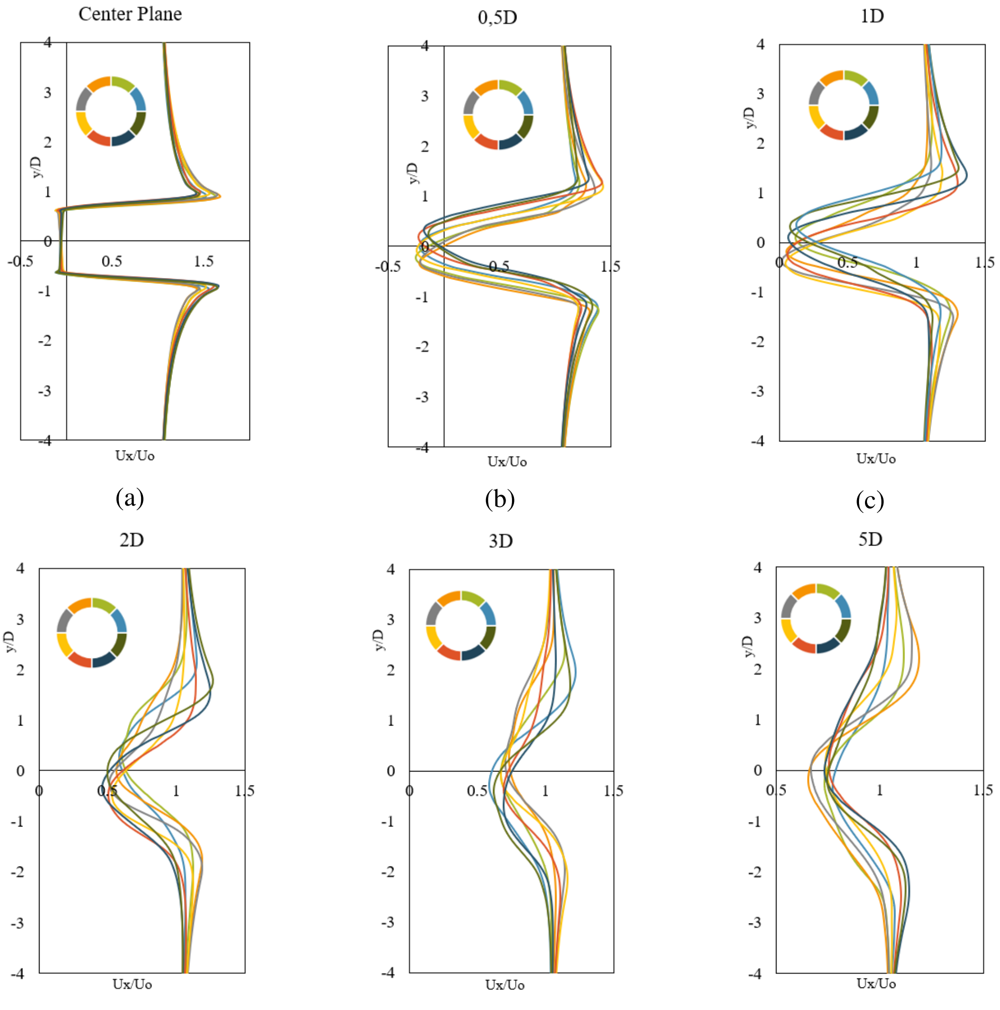

(a) (b) (c)

(d) (e) (f)

Figure C.2: Phase-averaged velocity profiles for the $k-\omega$ SST model

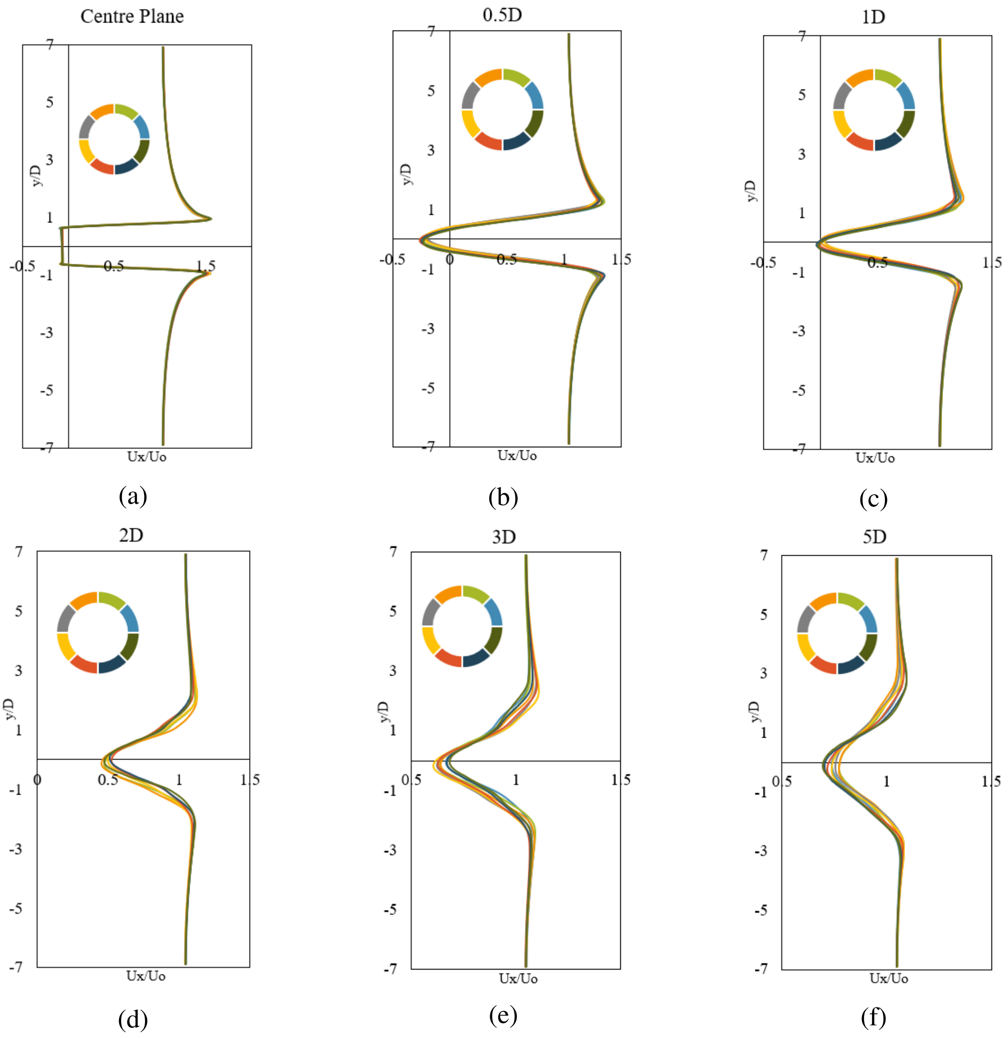

(a) (b) (c)

(d) (e) (f)

Figure C.3: Phase-averaged velocity profiles for the $k-\omega$ SSTLM model

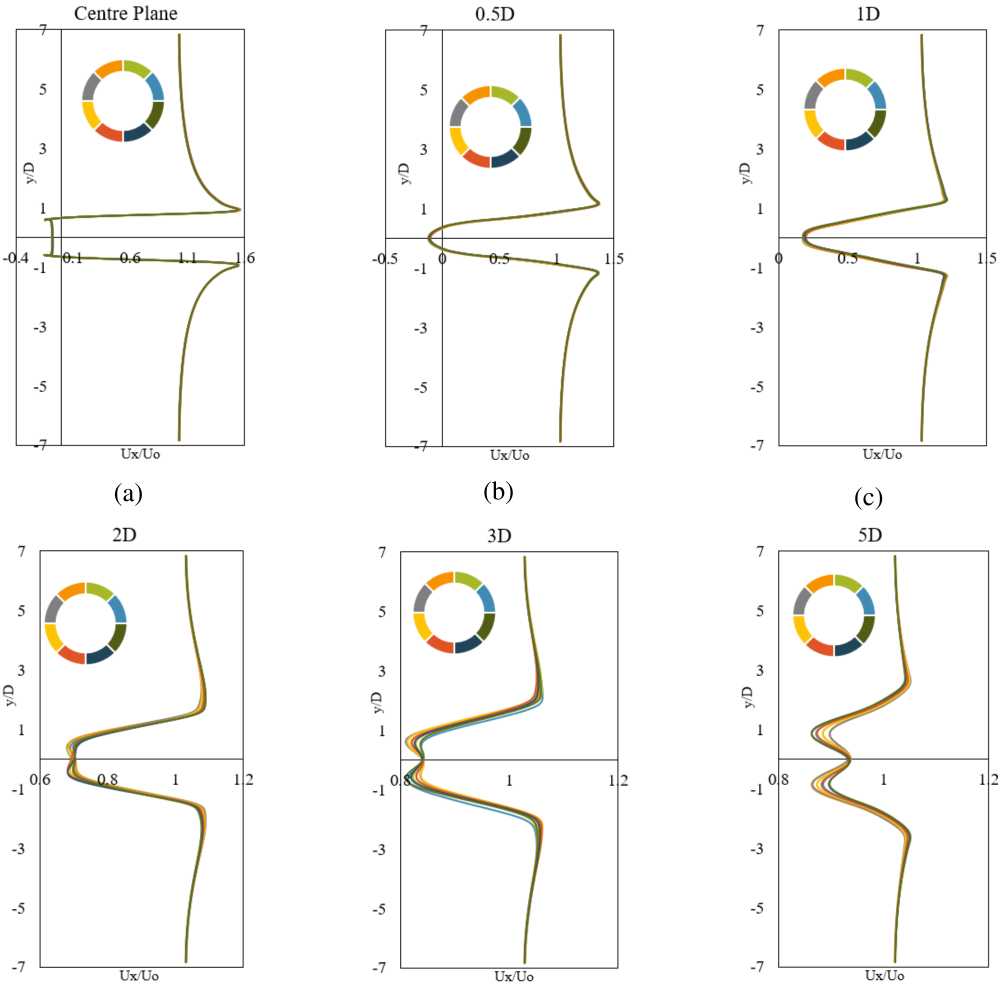

(a) (b) (c)

(d) (e) (f)

Figure C.4: Phase-averaged velocity profiles for the realizable $k-\varepsilon$ model

C.2 Reynolds Stress Turbulence Models

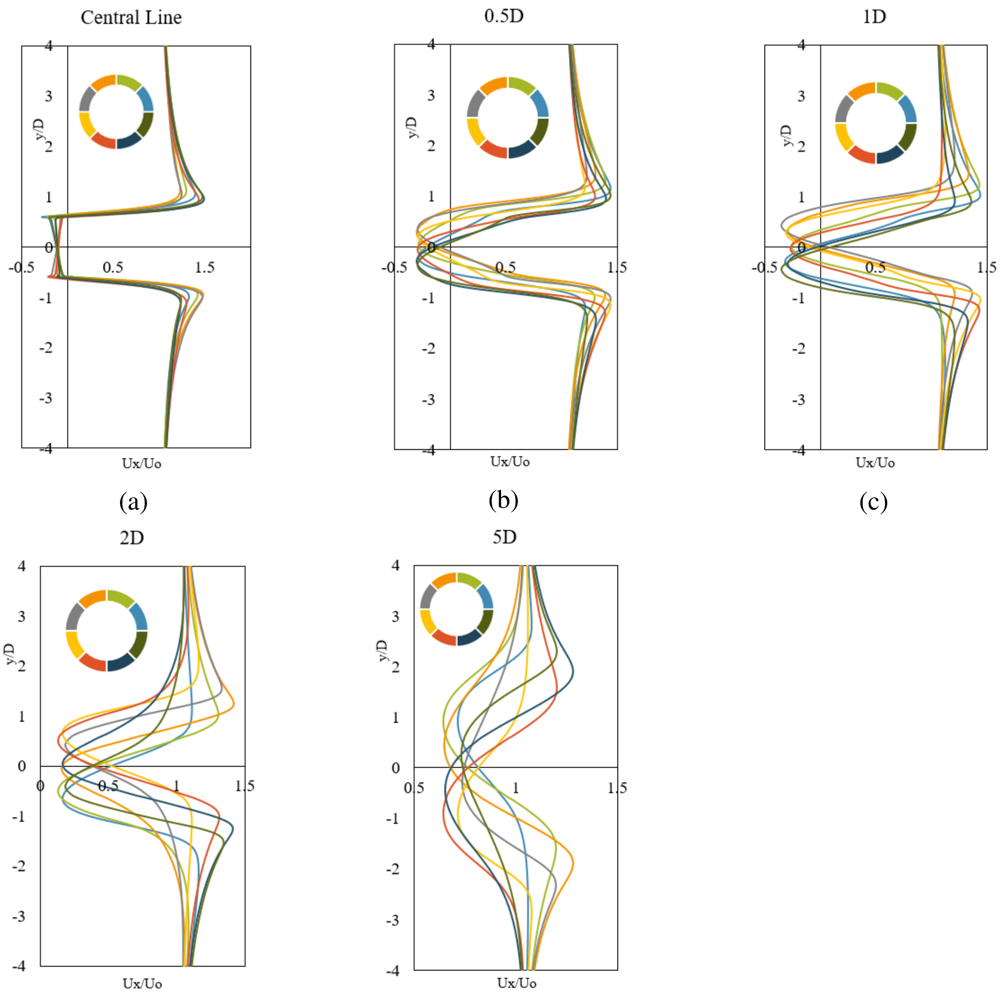

(a) (b) (c)

(d) (e)

Figure C.5: Phase-averaged velocity profiles for the LRR Reynolds Stress Turbulence Model

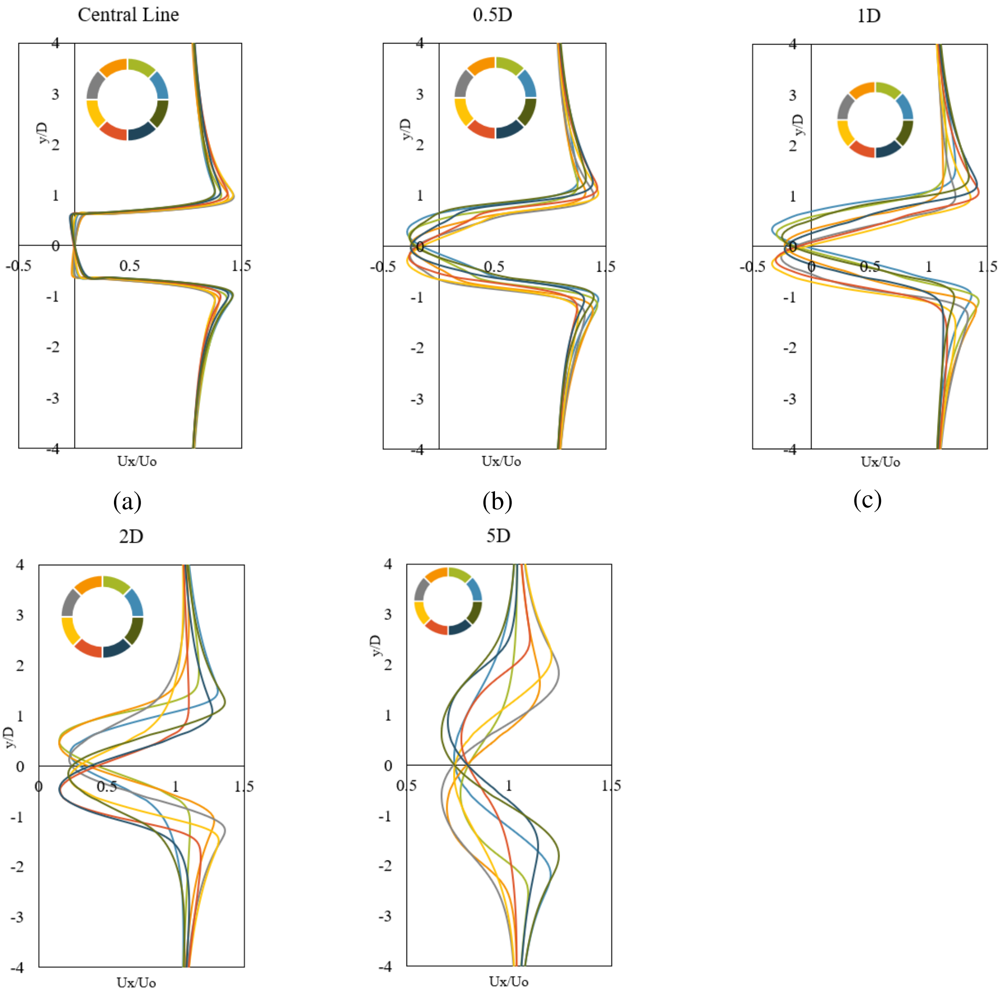

(a) (b) (c)

(d) (e)

Figure C.6: Phase-averaged velocity profiles for the SSG Reynolds Stress Turbulence Model

C.3 Low Reynolds Number Turbulence Models

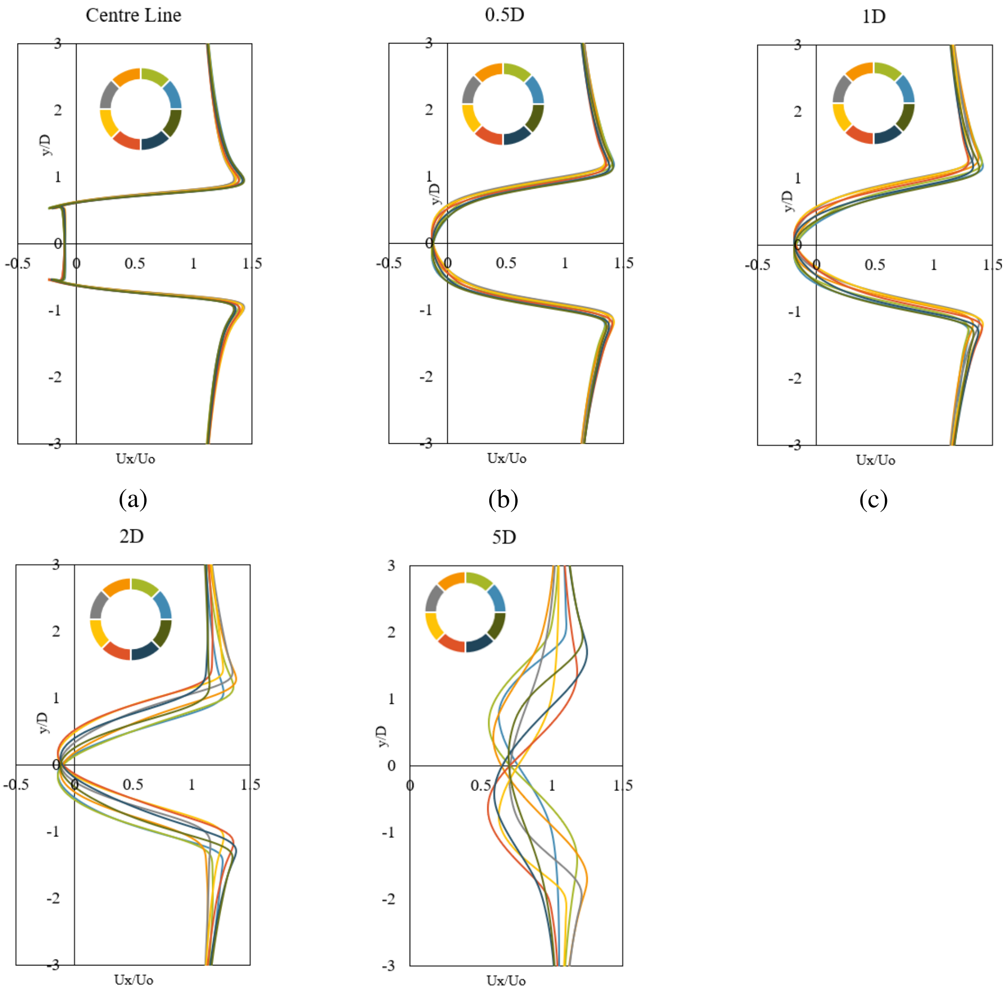

(a) (b) (c)

(d) (e)

Figure C.7: Phase-averaged velocity profiles for the Launder Sharma $k-\varepsilon$ turbulence model

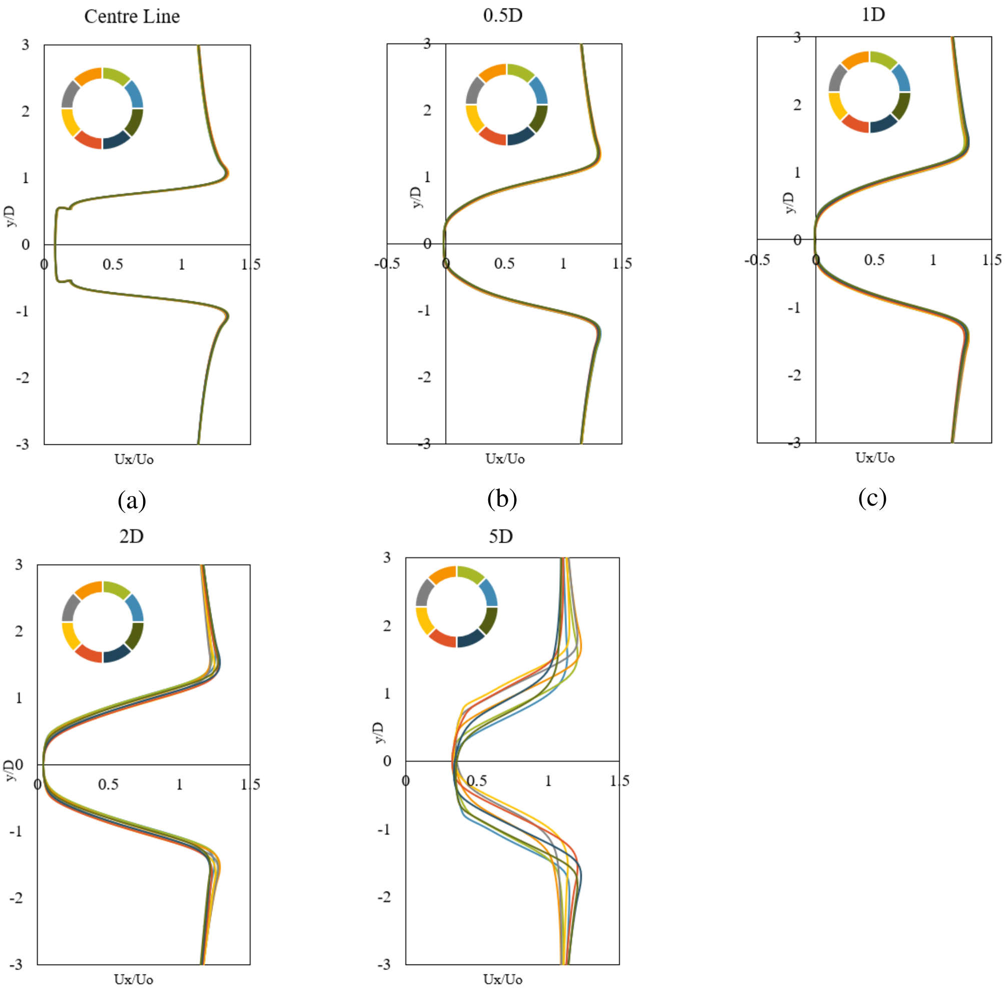

(a) (b) (c)

(d) (e)

Figure C.8: Phase-averaged velocity profiles for the Lien Cubic $k-\varepsilon$ turbulence model

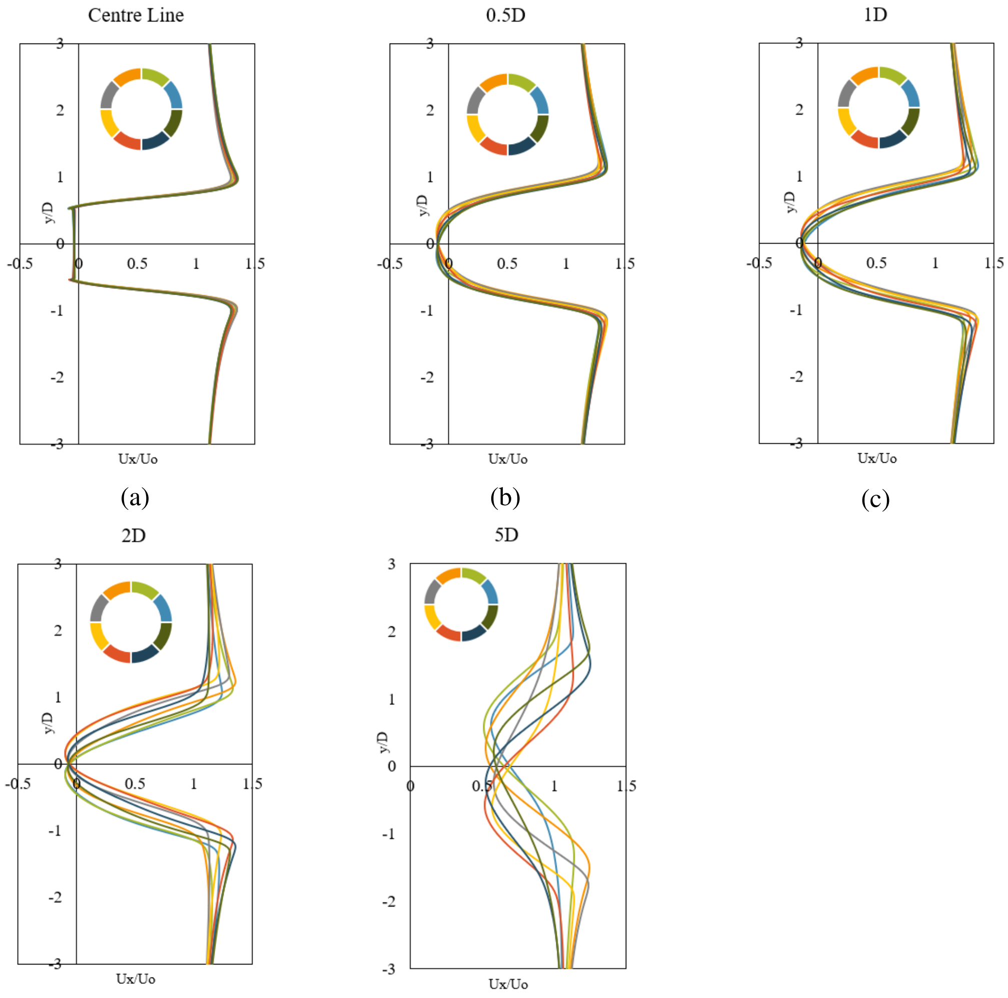

(a) (b) (c)

(d) (e)

Figure C.9: Phase-averaged velocity profiles for the Lam-Bremhorst $k-\varepsilon$ turbulence model

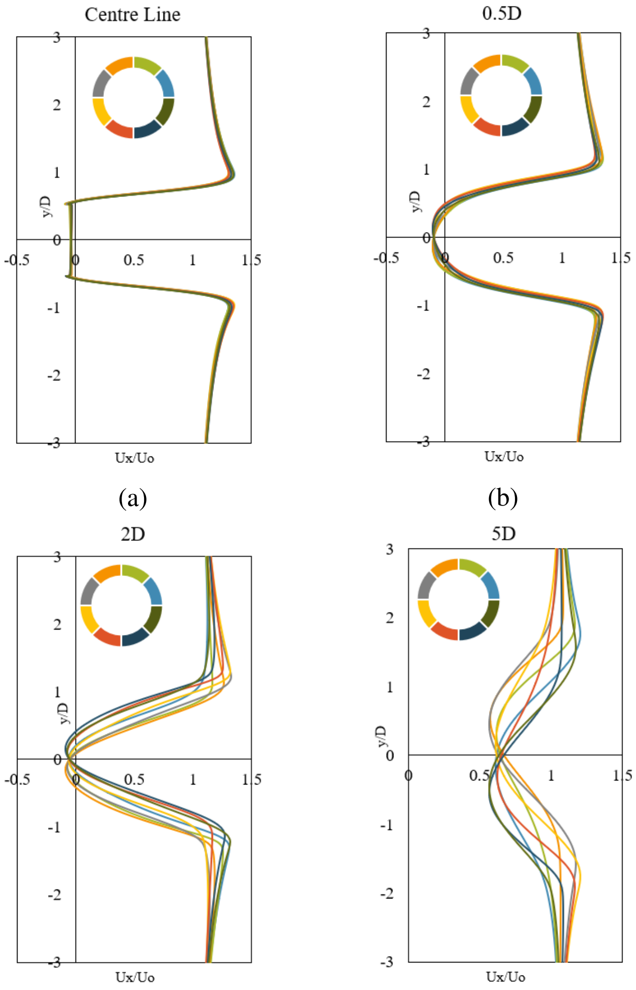

(a) (b) (c)

(d) (e)

Figure C.10: Phase-averaged velocity profiles for the Lien Leschziner $k - \varepsilon$ turbulence model

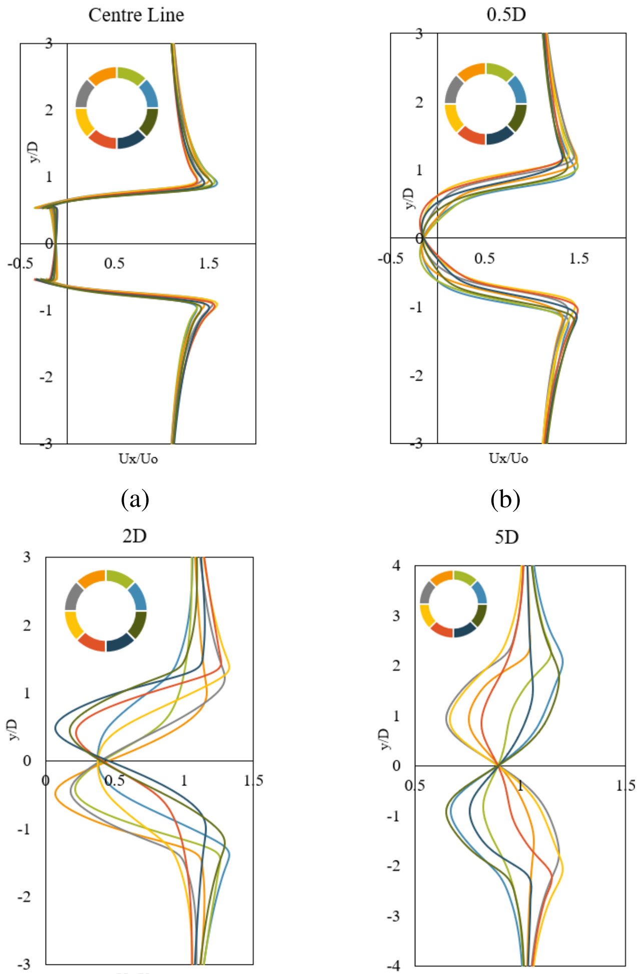

(a) (b) (c)

(d) (e)

Figure C.11: Phase-averaged velocity profiles for the $\overline{v^2} - f$ turbulence model

Appendix D

Reynolds Stresses Profiles

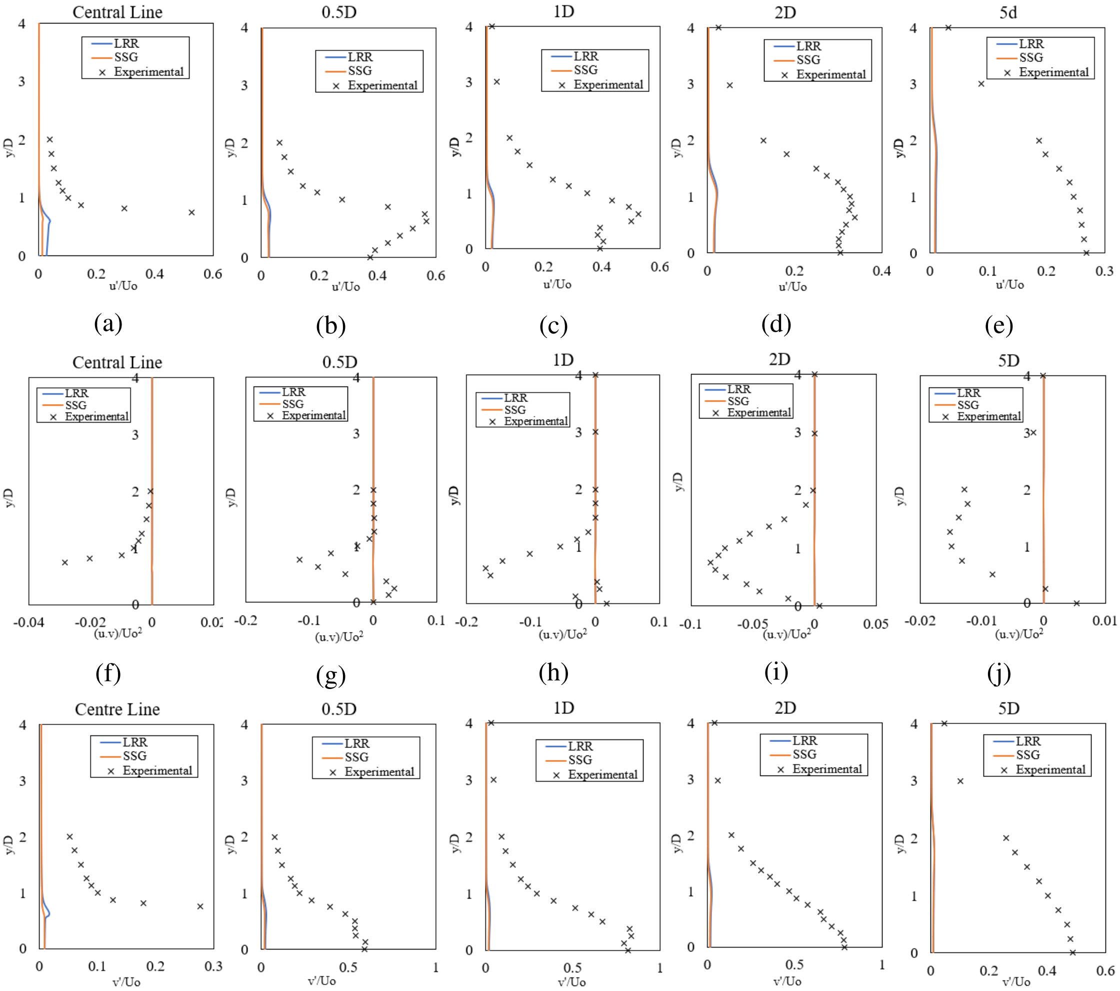

(a) (b) (c) (d) (e)

(f) (g) (h) (i) (j)

(k) (l) (m) (n) (o)

Figure D.1: Comparison of Reynolds stresses profiles between the LRR and SSG turbulence models and experimental data.

References

Franke, R. and Rodi, W. (1991). Calculation of vortex shedding past a square cylinder with various turbulence models. *Turbulent Shear Flows*, 8:189–204.

Jaw, S.-Y. (1998). *Fundamentals of Turbulence Modeling*. Taylor Fancis.

Launder, B. and Spalding, D. (1974). The numerical computation of turbulent flows. *Computer Methods in Applied Mechanics and Engineering*, 3:269–289.

Lee, I., Ryou, H., Lee, S., and Chae, S. (2000). Comparison of two-equation model and reynolds stress model with experimental data for the three-dimensional turbulent boundary layer in a 30 degree bend. *Journal of Mechanical Science and Technology*, 14(11):93–102.

Lien, F., Chen, W., and Leschziner, M. (1996). Low-reynolds-number eddy-viscosity modelling based on non-linear stress-strain/vorticity relations. *Engineering Turbulence Modelling and Experiments*, 3:91–100.

Lien, F.-S. and Kalitzin, G. (2001). Computations of transonic flow with $v^2 - f$ turbulence model. *International Journal For Numerical Methods in Fluids*, 22:53–61.

Liu, F. (2016). *A thorough description of how wall functions are implemented in openFOAM*. OpenSource Software.

Lyn, D., Einav, S., Rodi, W., and Park, J.-H. (1995). A laser-doppler velocimetry study of ensemble-averaged characteristics of the turbulent near wake of a square cylinder. *Journal of Fluid Mechanics*, 304:285–319.

Menter, F. (1992). Influence of freestream values on $k - \omega$ turbulence model predictions. *AIAA Journal*, 30(6):1657–1659.

Menter, F. (1994). Two-equation-eddy viscosity turbulence models for engineering applications. *AIAA Journal*, 32(8):1598–1605.

Menter, F. and Esch, T. (2001). Elements of industrial heat transfer predictions. *16th Brazilian congress of mechanical engineering*.

Menter, F., Langtry, R., S.Volker, and Huang, P. (2006). Transition modelling for general purpose cfd codes. *Flow, Turbulence and Combustion*, 77:277–303.

Minguez, M., Brun, C., Pasquetti, R., and Serre, E. (2011). Experimental and high-order les analysis of the flow in the near-wall region of a square cylinder. *International Journal of Heat and Fluid Flow*, 32:558–566.

Pantokratoras, A. (2016). Unconfined unsteady laminar flow of a power-law fluid across a square cylinder. *Fluids*.

Patel, F., Rode, W., and Scheuerer, G. (1984). Turbulence models for near-wall and low reynolds number flows: A review. *AIAA Journal*, 23(9):1308–1319.

Pope, S. (2000). *Turbulent Flows*. Cambridge University Press.

Sen, S., Mittal, S., and Biswas, G. (2011). Flow past a square cylinder at low reynolds number. *International Journal For Numerical Methods in Fluids*, 67:1160–1174.

Shih, T.-H., Liou, W., A. Shabbir, Z. Y., and Zhu, J. (1995). A new k-ε eddy viscosity model for high reynolds number turbulent flows. *Computer Fluids*, 24(3):227–238.

Sohanker, A., Davidson, L., and Norberg, C. (2000). Large eddy simulation of flow past a square cylinder: comparison of different subgrid scale models. *Journal of Fluids Engineering*, 122:39–47.

Speziale, C., Sarkar, S., and Gatski, T. (2000). Modelling the pressure-stain correlation of turbulence: an invariant dynamical systems approach. *Journal of Fluid Mechanics*, 227:245–272.

Trias, F., Gorobets, A., and Oliva, A. (2015). Turbulent flow around a square cylinder at reynolds number 22000: a dns study. *Computers and Fluids*, 123:87–98.

Versteeg, H. and Malalasekera, W. (2007). *An Introdution to Computational Fluid Dynamics*. Pearson Education Limited.

Wilcox, D. (2008). Formulation of the k-*omega* turbulence model revisited. *AIAA Journal*, 46(11):2823–2838.